Lrit1, a retinal transmembrane protein, regulates selective synapse formation in cone photoreceptor cells and visual acuity

膜蛋白質 Lrit1 は錐体視細胞選択的なシナプス形成に必須である

Laboratory for Molecular and Developmental Biology (Prof. Furukawa)
Institute for Protein Research
Graduate School of Frontier Biosciences
Osaka University

Akiko Ueno
2020.3.25

Abstract

In the vertebrate retina, cone photoreceptors play crucial roles in photopic vision by transmitting light-evoked signals to ON- and/or OFF-bipolar cells. However, the mechanisms underlying selective synapse formation in the cone photoreceptor pathway remain poorly understood. Here, I found that Lrit1, a leucine-rich transmembrane protein, localizes to the photoreceptor synaptic terminal and regulates the synaptic connection between cone photoreceptors and cone ON-bipolar cells. *Lrit1*-deficient retinas exhibit an aberrant morphology of cone photoreceptor pedicles, as well as an impairment of signal transmission from cone photoreceptors to cone ON-bipolar cells. Furthermore, I demonstrated that Lrit1 interacts with Frmpd2, a photoreceptor scaffold protein, and with mGluR6, an ON-bipolar cell-specific glutamate receptor. Additionally, *Lrit1*-null mice showed visual acuity impairments in their optokinetic responses. These results suggest that the Frmpd2-Lrit1-mGluR6 axis regulates selective synapse formation in cone photoreceptors and is essential for normal visual function.

Table of Contents

General introduction

In the central nervous system (CNS), which comprises the brain, retina, and spinal cord, various types of neurons connect with their specific partners through synapses and form neural circuits. Precise neural circuitry and synapse formation are essential for higher brain functions, such as memory, cognition, and learning. Synaptic defects during brain development are thought to be associated with psychiatric disorders, including schizophrenia and the autism spectrum (Penzes et al., 2011). Synaptic defects in the retina are related with night blindness (Furukawa et al., 2019). The retina is an excellent model to study synapse formation and function, because the retina forms relatively simpler neural circuits compared with those in other CNS regions. Retinal neurons form synapses at the fixed region, and synapses are easily visualized at a single synapse level.

The retina is a layered structure located at the back of the eye. The light from the outside is received by the retina and converted into an electric signal and then transmitted to the brain. The retina mainly consists of five layers: outer nuclear layer (ONL), inner nuclear layer (INL), ganglion cell layer (GCL), outer plexiform layer (OPL), and inner plexiform layer (IPL). It consists of five types of neurons and one type of glial cell; photoreceptor cells, bipolar cells, horizontal cells, amacrine cells, ganglion cells, and Muller glial cells (Bassett and Wallace, 2012) (Fig. G1 A). Photoreceptor cells, located in the outer part of the retina, are responsible for light reception in the retina. The signals received by photoreceptor cells are transmitted to the secondary neurons, bipolar cells, and subsequently from bipolar cells to the third neurons, retinal ganglion cells, located in the innermost part of the retina. Horizontal cells modify synaptic transmission between photoreceptor cells to bipolar cells in the OPL, and amacrine cells modify synaptic transmission between bipolar cells and ganglion cells in the IPL (Chaya et al., 2017;

Herrmann et al., 2011). Retinal ganglion cells transmit visual information received from bipolar cells and amacrine cells to the brain through their axons that form the optic nerve.

Photoreceptor cells are classified into two subtypes; rod photoreceptor, which functions in dim light vision and cone photoreceptor, which functions in day-light vision. (Kefalov, 2012). High-resolution human vision is mainly mediated by cone photoreceptors. Bipolar cells are also mainly classified into two subtypes, ON and OFF bipolar cells. Light stimulation depolarizes ON bipolar cells and hyperpolarizes OFF bipolar cells (Werblin and Dowling, 1969). Photoreceptor cells release an increased amount of glutamate in dark conditions than that in light conditions. Glutamate released from photoreceptor cells depolarizes OFF-bipolar cells by activating an ionotropic glutamate receptor (Morigiwa and Vardi, 1999). In contrast, glutamate hyperpolarizes ON-bipolar cells by closing the TRPM1 cation channel following activation of GRM6, an ON-bipolar cell-specific glutamate receptor (Koike et al., 2010a; Koike et al., 2010b; Shen et al., 2012; Xu et al., 2016).

Photoreceptor cell axon terminals connect with bipolar and horizontal cell dendritic terminals in the OPL. Bipolar cells, amacrine cells, and ganglion cells connect with each other in the IPL (Korenbrot, 2012; Masland, 2001). The synaptic structure in the retina has been well studied by using an electron microscope. In the OPL, two horizontal and ON-bipolar cell dendritic terminals invaginate the photoreceptor axon terminal. While rod photoreceptor synaptic terminals (spherule) contain only one invagination site, cone photoreceptor synaptic terminals (pedicle) contain multiple invagination sites (Fig. G1B, C). The cone pedicle can be identified easily, because it is larger than the rod spherule. Rod and cone photoreceptor cells form selective synaptic connections with different types of bipolar cells. Cone photoreceptors are connected to two types of bipolar cells, ON- and

OFF-bipolar cells. In contrast, rod photoreceptors are connected to ON-bipolar cells only. OFF-bipolar cell dendritic terminals make flat, non-invaginating contacts with cone photoreceptor axon terminals (D'Orazi et al., 2014; Wassle, 2004) (Fig. G1B). A specialized electron-dense plate-like structure, “ribbon”, is observed near the invagination terminals of the photoreceptor cell. The synaptic ribbon tethers 100 or more synaptic vesicles to the surface (Parsons and Sterling, 2003). Vesicles tethered to the ribbon enable acute and sustained neurotransmitter releases (Heidelberger et al., 2005; Sterling and Matthews, 2005). Synaptic ribbons are observed in the ear and the retina, which are sensory organs that require rapid, large-signal transmission. (Matthews and Fuchs, 2010; Penzes et al., 2011; Sterling and Matthews, 2005; Wan et al., 2014). Cone photoreceptor synapse formation begins at around the postnatal day 4 (P4) in mice, while rod photoreceptor synapse formation begins at around P8, and both are completed until about P15 (Blanks et al., 1974; Rich et al., 1997; Sherry et al., 2003).

Previous studies reported that various molecules are involved in or regulate synapse formation in the brain and the retina._In the retina, several molecules essential for photoreceptor synapse formation have been identified (Furukawa et al., 2019) (Fig. G2). For example, Pikachurin, a secreted extracellular matrix protein, is localized in the photoreceptor synaptic cleft and regulate photoreceptor-ON-bipolar cell synapse formation. Pikachurin binds to Dystroglycan at photoreceptor axon terminals and recruits GPR179 to the ON-bipolar cell dendritic terminals (Orlandi et al., 2018; Sato et al., 2008). *Pikachurin*$^{-/-}$ mice display synaptic transmission defects from photoreceptor cells to ON-bipolar cells, and the electron microscope analysis shows a defect of the synaptic structure. Recently, a cell adhesion protein, Elfn1, regulating rod photoreceptor-ON-bipolar cell selective synapse formation was reported. Elfn1 is localized to rod photoreceptor axon

terminals and interacts in trans with Grm6 localized on ON-bipolar cell dendritic terminals (Cao et al., 2015). *Elfn1*$^{-/-}$ mice show synaptic transmission defects from rod to ON-bipolar cells but show a normal synaptic transmission from cone to ON-bipolar cells. On the other hand, little is known about the mechanisms of selective synapse formation between cone photoreceptor cells and ON-bipolar cells. In the brain, several cell adhesion proteins and secreted proteins, such as Neulexin, Neuroligin, Ephrin, SynCAM, LRRTM , Cnln1, and Gpc4, have been reported as molecules that regulate synapse formation. (Condomitti et al., 2018; Dalva et al., 2000; Matsuda et al., 2010; Penzes et al., 2011; Robbins et al., 2010; Sudhof, 2008; Uemura et al., 2010). Cell adhesion proteins and secreted extracellular matrix proteins mainly regulate synapse formation both in the brain and the retina. Although synapse formation mechanisms are well studied as described adobe, the mechanism and molecules underlying selective synapse formation, such as neuron subtype-specific synapse formation, are poorly understood in the CNS.

Introduction

Vision in vertebrates is initiated by rod and cone photoreceptor cells. While rod photoreceptors are highly sensitive and responsible for low light vision, cone photoreceptors are less sensitive but can respond to a broad range of light intensities of specific wavelengths, and are responsible for daylight and color vision. Human high resolution vision is mainly mediated by cone photoreceptors. The vertebrate retina processes image-forming visual information detected by cone and rod photoreceptors through parallel ON and OFF pathways (Schiller, 1992, 2010). The parallel ON and OFF pathway system for visual information processing is evolutionally conserved from fly to human (Behnia et al., 2014). The segregation of the ON and OFF pathways begins with the divergence of cone photoreceptor signals to ON-bipolar cells and OFF-bipolar cells (Werblin and Dowling, 1969). Cone bipolar cells, both ON and OFF types, receive signal inputs from cone photoreceptors and directly connect to retinal ganglion cell dendrites in the inner plexiform layer (IPL). In contrast, rod bipolar cells are only ON-bipolar cells and their axonal terminals extend to the deepest region of the IPL. Rod photoreceptors transmit only ON pathway signals. ON- and OFF-bipolar cells are distinguished by electrophysiological and anatomical features. ON-bipolar cells express a metabotropic glutamate receptor 6 (mGluR6, Grm6) on their dendrites (Nakanishi et al., 1998). The ON-bipolar dendrite has a single invaginating contact with a photoreceptor terminal (D'Orazi et al., 2014). On the other hand, OFF-bipolar cells express ionotropic GluRs (AMPA/Kainate receptors), glutamate-gated cation channels, on their dendrites (Morigiwa and Vardi, 1999). The OFF-bipolar dendrite makes multiple flat contacts with a cone photoreceptor terminal (D'Orazi et al., 2014). Under dark conditions, the neurotransmitter glutamate is released at a high rate from cone terminals and depolarizes

OFF-bipolar cells through ionotropic GluR, whereas glutamate hyperpolarizes ON-bipolar cells through Grm6 activation leading to the closure of the TRPM1 cation channel (Koike et al., 2010a). The axon terminals of ON-bipolar cells terminate in the inner three-fifths of the IPL, whereas those of OFF-bipolar cells terminate in the outer two-fifths of the IPL.

Photoreceptor cells connect with interneurons, bipolar cells, and horizontal cells, through a specialized synapse called the ribbon synapse. The ribbon synapse contains invaginations into which bipolar dendritic tips and horizontal cell processes are inserted (Sterling and Matthews, 2005; tom Dieck and Brandstatter, 2006). For the proper formation of photoreceptor synaptic invagination, a complex composed of an extracellular matrix protein, Pikachurin, and a membrane glycoprotein, Dystroglycan, is required (Kanagawa et al., 2010; Omori et al., 2012; Sato et al., 2008). Dystroglycan localizes to the photoreceptor synaptic terminal and Pikachurin is localized in the synaptic cleft between photoreceptors and ON-bipolar cells. Loss of either Pikachurin or Dystroglycan causes the absence of the proper intrusion of ON-bipolar cell dendritic tips into photoreceptor synaptic terminals, leading to an impaired synaptic connection between photoreceptor and ON-bipolar cells and a significant delay of the signal transmission from photoreceptor to ON-bipolar cells.

The transmembrane protein Elfn1 is expressed in the globus pallidus and interneurons in the cortex and hippocampus of the developing mouse brain (Dolan et al., 2007). Elfn1 is involved in synaptic function and synapse formation of interneurons in the mouse hippocampus (Sylwestrak and Ghosh, 2012; Tomioka et al., 2014). It was recently reported that Elfn1 is expressed in rod photoreceptors and localizes at the rod synaptic terminals in the mouse retina, and that Elfn1 is necessary for synapse formation between

rod photoreceptors and rod bipolar cells through binding *in trans* to ON-bipolar-specific Grm6 (Cao et al., 2015). Hence, the molecular mechanisms underlying synapse formation of rod photoreceptors are being gradually clarified. On the other hand, molecular mechanisms for synaptic formation of cone photoreceptors remain largely unknown.

In the current study, I searched for molecules essential for photoreceptor synapse formation and maintenance, and identified a transmembrane protein of unknown function, Lrit1. Lrit1 localizes to photoreceptor synaptic terminals. I investigated its biological functions using *Lrit1*-null mice, revealing that *Lrit1* regulates cone photoreceptor synapse formation, proper synaptic transmission between cone photoreceptors and bipolar cells, and development of normal visual acuity. Lrit1 interacts with Grm6 and Frmpd2, a photoreceptor scaffolding protein. The Frmpd2-Lrit1-Grm6 axis is part of my proposed mechanism for regulation of the selective synaptic formation of cone photoreceptors.

Results

Isolation of *Lrit1* and *Lrit2*

To identify genes regulating retinal photoreceptor synapse formation, I searched for transmembrane, membrane-associated, or extracellular proteins enriched in photoreceptor cells (Fig. S1A). It was previously reported that microarray analysis of the *Otx2* conditional knockout (CKO) mouse retina lacking Otx2 in the retina was performed (Nishida et al., 2003; Omori et al., 2011). Since cell fate conversion from photoreceptor cells to amacrine-like cells occurs in the *Otx2* CKO retina, genes enriched in photoreceptor cells decrease in the *Otx2* CKO retina. I first selected candidate genes, which encoded transmembrane, membrane-associated, or extracellular proteins, among 716 genes substantially decreased in the *Otx2* CKO retina. For these candidate genes, I carried out *in silico* analysis based on EST expression patterns, evolutionary conservation, and protein domains. Then, I performed an *in situ* hybridization screen to observe the actual expression patterns of candidate genes in the mouse retina. I ultimately selected 11 candidate genes regulating photoreceptor synapse formation. Among these candidate genes, I focused on two genes, *Lrit1* and *Lrit2,* in the current study. Although retina-specific expression of the rat *Lrit1* homolog (*Pal*) was reported (Gomi et al., 2000), *Lrit1* function has not yet been reported. *Lrit1* encodes a 624 amino acid protein, containing an N-terminal signal sequence, five Leucine-rich repeat domains, an Immunoglobulin (Ig)-like domain, a Fibronectin 3 (FN3) domain, and a transmembrane domain, whereas, *Lrit2* encodes a 549 aa protein containing domains similar to those of the Lrit1 protein, except for a PDZ-binding motif (Fig. 1A). A PDZ-binding motif is present in the C-terminal intracellular domain of Lrit1, but not in Lrit2. *Lrit1* and *Lrit2* genes are evolutionarily

conserved through vertebrates including zebrafish and humans.

Lrit1 and Lrit2 are expressed in retinal photoreceptor and bipolar cells

To examine the tissue specificities of *Lrit1* and *Lrit2* expression, I performed a northern blot analysis with adult mouse tissues. I observed a single 5.1-kb *Lrit1* band and a single 2.7-kb *Lrit2* band in the mouse retina, but not in other tissues examined (Fig. S1B). I then carried out *in situ* hybridization analysis using developing and mature mouse retinal sections (Fig. S1C). At P3, the *Lrit1* signal was below detection level. *Lrit1* expression was first detected at P9 in the outer nuclear layer (ONL), the photoreceptor cell layer, and the inner nuclear layer (INL), which contains bipolar cells. It is at this stage that synapse formation in photoreceptor cells begins (Blanks et al., 1974; Rich et al., 1997; Sherry et al., 2003). At P21, the expression level of *Lrit1* decreased, but a steady signal continued to be observed in the photoreceptor cell layer and bipolar cell layer. *Lrit2* was first detected in the ONL and INL at P21 (Fig. S1C). These results show that *Lrit1* and *Lrit2* are predominantly expressed in developing photoreceptor and bipolar cells. As I will describe later, since I found that Lrit2 is dispensable for photoreceptor synapse formation, I will mainly describe the analysis of Lrit1.

Lrit1 localizes to photoreceptor synapses in the OPL

To investigate Lrit1 localization in photoreceptor and bipolar cells, I raised an antibody against the Lrit1 protein. I immunostained mouse retinal sections at 1 month old (1M) using the anti-Lrit1 antibody with an anti-PKC-alpha (PKCα) antibody that stains rod ON-bipolar cells (Fig. 1B). Lrit1 localized to the dendritic tips of ON-bipolar cells with a punctated pattern in the OPL, and to the axonal terminals of ON and OFF bipolar

cells in the IPL (Fig. 1B, S1D). To examine Lrit1 localization in the OPL more precisely, I analyzed the localization of Lrit1 by co-immunostaining with the photoreceptor synaptic terminal marker Pikachurin (Sato et al., 2008) and synaptic ribbon marker Ctbp2 (Wassle et al., 2009). Rod photoreceptor synaptic terminals exhibited single Ctbp2-positive signals, whereas cone photoreceptor synapses displayed clusters of multiple Ctbp2-positive signals (Fig. 1C). Lrit1 signals were observed close to photoreceptor terminals between the horseshoe-like Ctbp2-positive synaptic ribbons and synaptic clefts stained with Pikachurin both in rod and cone photoreceptor axon terminals in the OPL (Fig. 1C), suggesting that Lrit1 in the OPL is likely to be produced by photoreceptor cells. I then co-immunostained the 1M retina with antibodies against Lrit1 and ON-bipolar cation channel Trpm1, photoreceptor synaptic terminal proteins Dystroglycan (DG), or Elfn1 (Fig. 1D). Lrit1 signals were detected in the sub-regions of photoreceptor synaptic terminals partially overlapping Trpm1, DG, and Elfn1 signals. This result suggests that Lrit1 localizes at rod and cone photoreceptor axon terminals encountering ON-bipolar dendritic tips but in different sub-regions than DG and Elfn1. To explore Lrit1 localization in photoreceptor synaptic terminals more precisely, I performed a multicolor three-dimensional structured illumination microscopy (3D-SIM) analysis. In the 3D-SIM analysis, I confirmed that Lrit1 localizes to a narrow membrane region just outside of the synaptic ribbon, which is confined between two bipolar cell dendritic tips (Fig. 1E).

Lrit1 is necessary for the proper formation of cone photoreceptor synapses

To investigate the possible role of *Lrit1* in photoreceptor synapse formation and/or maintenance, I generated *Lrit1*-null mice ($Lrit1^{gt/gt}$) by targeted gene disruption. A gene-trap insertion containing a splice acceptor-IRES-*LacZ* cassette in intron 1 of the *Lrit1* loci

interrupted the production of *Lrit1* mRNA after exon 2 (Fig. S1E). In the *Lrit1*$^{gt/gt}$ retina, no substantial post-exon 2 mRNA was detected by RT-PCR (Fig. S1F). In addition, the Lrit1 immunofluorescent signal in the *Lrit1*$^{gt/gt}$ retina was below detection level (Fig. 2A, S1G). *Lrit1*$^{gt/gt}$ mice were viable and fertile, and showed no gross morphological abnormalities. To examine the integrity of photoreceptor ribbon synapses in the *Lrit1*$^{gt/gt}$ retina, I stained retinal sections with rhodamine-labeled peanut agglutinin (PNA, a cone photoreceptor synapse marker) or antibodies against Pikachurin, Grm6 (an ON-bipolar dendritic tip marker), Lrit3 (an ON-bipolar dendritic tip marker), Ctbp2, PKCα, Znp1 (an OFF-bipolar dendritic marker), and Calbindin (a horizontal cell process marker). I observed that PNA patterns were irregular in *Lrit1*$^{gt/gt}$ retinas (Fig. 2B), but no substantial change was detected for other markers tested between wild-type (WT) control and *Lrit1*$^{gt/gt}$ retinas (Fig. 2A, S1H). To investigate the cone synaptic terminal abnormality in *Lrit1*$^{gt/gt}$ retinas in more detail, I performed flat-mount staining of the retina using PNA. In this analysis, morphologies of cone synapse clusters are more clearly visible compared to those in frozen sections. I found that the number of diffused, shrunken, or fused cone synapse clusters significantly increased in *Lrit1*$^{gt/gt}$ retinas (Fig. 2C, D). To measure the exact volume of cone synapse terminals, I performed 3D-SIM analysis using flat mount PNA-stained *Lrit1*$^{gt/gt}$ retinas. I found that the volume of cone synaptic terminals stained with PNA in the OPL of the *Lrit1*$^{gt/gt}$ retina was reduced to 50.7% of that in control mice (Fig. 2E), indicating that cone synaptic terminals are smaller in the *Lrit1*$^{gt/gt}$ retina, probably because of synaptic cluster shrinkage and morphological changes. To confirm this result, I performed flat-mount immunostaining using an antibody against Arrestin3, a cone pedicle marker (Keeley et al., 2013), and quantified Arrestin3-stained cone pedicle areas in the *Lrit1*$^{gt/gt}$ retina. Average cone pedicle size in the *Lrit1*$^{gt/gt}$ retina was reduced

to 72.3% of that in the WT retina (Fig. 2F, G). These results suggest that *Lrit1* is required for proper morphological formation of cone synaptic terminals. In contrast, I observed no morphological change in rod photoreceptor synaptic terminals immunostained with anti-Pikachurin and anti-Ctbp2 antibodies (Fig. 2A, S1H), suggesting that Lrit1 regulates specifically proper cone photoreceptor synapse formation. To quantify the regularity of cone pedicle distribution in the *Lrit1*$^{gt/gt}$ retina, I analyzed the distribution using the Voronoi domain regularity index, which is commonly used to analyze mosaic distribution of retinal cells (Kay et al., 2012). In this analysis, I observed no significant difference between WT and *Lrit1*$^{gt/gt}$ retinas (Fig. S1I).

Lrit1 is required for signal transmission between cone photoreceptor and cone ON-bipolar cells

To elucidate the physiological role of *Lrit1 in vivo*, I measured electroretinograms (ERGs) of *Lrit1*$^{gt/gt}$ mice under dark-adapted (scotopic) and light-adapted (photopic) conditions. First, the scotopic ERGs elicited by four different stimulus intensities (-4.0, -3.0, -1.0, +1.0 log cd sm^{-2}) of white light were evaluated for WT control and *Lrit1*$^{gt/gt}$ mice (Fig. 3A-C, S2A-D). The amplitude of the scotopic ERG a-wave, which originates mainly from the activity of rod photoreceptor cells, showed no obvious change in *Lrit1*$^{gt/gt}$ mice compared to the control mice (Fig. 3A, S2A). I found that the implicit time of the scotopic ERG b-wave, which is an indication of the speed of the transduction process between photoreceptor and bipolar cells, is slightly delayed only at stimulus intensity of 1.0 log cd sm^{-2} as compared to the WT (Fig. 3A, B, S2D).

Next, I analyzed light-adapted (photopic) ERGs elicited by four different stimulus intensities (-0.5, 0, +0.5, +1.0 log cd sm^{-2}) of white light in control and *Lrit1*$^{gt/gt}$ mice (Fig.

3D-H, S2E-H). In the *Lrit1*$^{gt/gt}$ mice, the implicit times of photopic ERG b-waves, which represent electrical potentials from cone ON-bipolar cells activated by cone photoreceptor cells, significantly increased at stimulus intensities of -0.5, 0, 0.5 and 1.0 log cd sm^{-2}, and the amplitudes of the photopic ERG b-waves significantly decreased at stimulus intensities of 0.5 and 1.0 log cd sm^{-2} (Fig. 3D, E, G, S2F, H) compared to controls. In contrast, I observed no significant differences in implicit times and amplitudes of scotopic and photopic ERG a-waves between control and *Lrit1*$^{gt/gt}$ mice, indicating that phototransduction cascades in rod and cone photoreceptor cells are not affected in *Lrit1*$^{gt/gt}$ mice (Fig. 3C, F, H, S2A, C, E, G). These results suggest that synapse transmission from cone photoreceptors to cone ON-bipolar cells was impaired in *Lrit1*$^{gt/gt}$ mice. The slight delay of the implicit time of scotopic ERG b-waves in *Lrit1*$^{gt/gt}$ mice may be due to a carryover from cone photoreceptor to rod photoreceptor in ERG, because only the implicit time was affected and only at the strongest light stimulus intensity of 1.0 log cd sm^{-2}, which may stimulate cone photoreceptors. I recorded ERG d-waves to explore whether *Lrit1* loss affects OFF pathway function. The ERG d-wave was recorded under photopic conditions using long duration flashes with the injection of a glutamate analogue, APB (L-2-amino-4-phosphonobutyric acid) to remove ON pathway activity (Shirato et al., 2008). I did not observe significant changes in ERG d-wave amplitudes elicited by 100 or 200 msec stimulus duration between WT and *Lrit1*$^{gt/gt}$ mice (Figure S2I, J). This result suggests that *Lrit1* is dispensable for OFF pathway function.

It was previously reported that both *Pikachurin*$^{-/-}$ and retina-specific *Dystroglycan*-deficient mice exhibited a significant delay in implicit b-wave times in both photopic and scotopic ERGs (Omori et al., 2012; Sato et al., 2008). In *Dystroglycan*- or *Pikachurin*-null retinas, there was impairment of the invagination of bipolar cell terminals to

photoreceptor cell ribbon synapses. To examine whether the *Lrit1*$^{gt/gt}$ retina, which showed an implicit time delay of b-wave, possessed ultrastructural changes of photoreceptor ribbon synapses, I carried out electron microscopic analysis. In this analysis, I observed normal invagination and triad structures in the OPL of the *Lrit1*$^{gt/gt}$ retinas and detected no obvious difference between control and *Lrit1*$^{gt/gt}$ retinas (Fig. S2K, L). These results show that *Lrit1* is necessary for the establishment of the proper cluster structure of cone synapse pedicles, but is not involved in the formation of photoreceptor synaptic invagination, as is Pikachurin. To examine whether *Lrit1* loss affects cone photoreceptor ribbon numbers, I quantified the number of cone synaptic ribbons in WT and *Lrit1*$^{gt/gt}$ retinas stained with anti-Ctbp2 antibody and rhodamine-labeled PNA. I observed that the number of synaptic ribbons in cone photoreceptor was unaltered between WT and *Lrit1*$^{gt/gt}$ retinas (Fig. S2M).

Lrit1 in photoreceptor cells is responsible for the OPL phenotype

To test the possibility that *Lrit1* in bipolar cells affects cone photoreceptor synapse formation and/or the ERG b-wave amplitude and implicit time, I generated *Lrit1* conditional knockout (CKO) mice, which lack *Lrit1* specifically in ON-bipolar cells, by crossing *Lrit1*$^{fl/fl}$ mice, in which exon 2 is floxed, with the *Grm6-Cre* BAC transgenic mice, in which Cre recombinase is specifically expressed in ON-bipolar cells (Fig. S3A-C), since *Lrit1* is expressed both in photoreceptor and bipolar cells in the retina (Fig. S1C). In *Lrit1* CKO mice, the Lrit1 signal was observed in photoreceptor synapses in the OPL but disappeared in ON-bipolar cell axon terminals in the IPL (Fig. S3D). I found that *Lrit1* CKO mice show normal morphology of cone synapse terminals (Fig. S3E) and no obvious difference in ERG responses compared to those of control mice (Fig. S3F-H),

suggesting that Lrit1 expression in photoreceptor cells, but not in bipolar cells, is required for accurate synaptic transmission and formation of cone synaptic terminal structures in the OPL.

Lrit2 is dispensable for photoreceptor synapse formation

To investigate *Lrit2* function in the retina, I generated *Lrit2* mutant mice carrying a 1-bp insertion by CRISPR/Cas9–mediated genome editing in exon 2 of *Lrit2*, resulting in a premature stop codon 51 aa after the N-terminus (Fig. S4A, B). *Lrit2*$^{-/-}$ mice were viable and fertile, and showed no gross morphological abnormalities. I stained the retina with PNA to observe the integrity of cone photoreceptor synapses, and observed that the morphology of the cone synaptic terminals was not affected in *Lrit2*$^{-/-}$ retinas compared with that in WT control mouse retinas (Fig. S4C). *Lrit2*$^{-/-}$ mice showed normal ERG responses (Fig. S4D, E). I observed no obvious change between WT control and *Lrit2*$^{-/-}$ retinas for synapse marker antibodies against Ctbp2, PKCα, Calbindin, Grm6, Pikachurin, and Lrit1 (Fig. S4F). These results suggest that *Lrit2* is not essential for photoreceptor synapse formation.

Because of the high similarity of the amino acid sequences between Lrit1 and Lrit2 proteins as well as their similar tissue distribution and adjacent genomic loci, I supposed that there might be functional redundancy between these two genes. The Lrit3 protein is also highly homologous with Lrit1 and Lrit2 proteins, however, Lrit3 is expressed and functions in ON-bipolar cells (Neuille et al., 2015; Zeitz et al., 2013). To examine the possible functional redundancy between *Lrit1* and *Lrit2*, I generated *Lrit1/2* double KO (DKO) mice by targeted gene disruption. The genomic loci of *Lrit1* and *Lrit2* are adjacent on mouse chromosome 14 (Fig. S5A). I deleted exon 2 to 4 of *Lrit1* and exon 1 and exon

2 of *Lrit2*, resulting in *Lrit1*- and *Lrit2*-double null alleles (Fig. S5A). I confirmed that expression of both *Lrit1* and *Lrit2* mRNAs were disrupted in *Lrit1/2* DKO retinas (Fig. S5B). Immunofluorescent analysis showed that the Lrit1 signal was absent in the *Lrit1/2* DKO retina (Fig. S5C). In the *Lrit1/2* DKO mice, I observed a cone photoreceptor synapse defect in flat-mount PNA staining, similar to that observed in *Lrit1*-null retinas (Fig. S5D). I found no obvious change of immunostaining pattern using synapse markers including Ctbp2, Pikachurin, Grm6, Elfn1, PKCα, Zpn1 and Calbindin in between control and *Lrit1/2* DKO retinas (Fig. S5E). The ultrastructure of the photoreceptor ribbon synapse was not affected in the *Lrit1/2* DKO retina, compared with that in control retina (Fig. S5F). Prolongation of the implicit time and amplitude reduction of photopic ERG b-waves were observed in *Lrit1/2* DKO mice (Fig. S6A-E). These *Lrit1/2* DKO phenotypes were almost the same as those of $Lrit1^{gt/gt}$ mice, suggesting that *Lrit1* and *Lrit2* are not functionally redundant for photoreceptor synapse formation.

To examine whether the aberrant morphology of cone photoreceptor axon terminals in the *Lrit1/2* DKO retina are due to a defect in development or maintenance, I stained control and *Lrit1/2* DKO retinas with PNA at P11 and P14 (Fig. S6F). I observed that PNA stained cone terminals less intensely in the *Lrit1/2* DKO retina compared with the control retina, implying that the development of cone photoreceptor axon terminals is impaired in the *Lrit1/2* DKO retina.

Lrit1 interacts with Lrit2 and Grm6

Lrit1 and Lrit2 are leucine-rich repeat (LRR)-containing transmembrane proteins (LRRPs). LRRPs have been reported to homo- or hetero-dimerize through the LRR domain in the extracellular region (Bella et al., 2008; Jin et al., 2007). Since Lrit1-3

possess the LRR domains, I speculated that Lrit1 might interact with Lrit2 and/or Lrit3. To test this possibility, I performed an immunoprecipitation assay. I transfected a FLAG-tagged Lrit1 (Lrit1-FLAG) expression plasmid with HA-tagged Lrit1, Lrit2 or Lrit3 expression plasmids (Lrit1-HA, Lrit2-HA, Lrit3-HA) into HEK293 cells, and immunoprecipitated HEK293 cell lysates with an anti-FLAG antibody. I observed that Lrit1-HA and Lrit2-HA are immunoprecipitated with the anti-FLAG antibody (Fig. 4A), suggesting that Lrit1 interacts with itself or Lrit2. In contrast, I observed a very faint band of Lrit3-HA immunoprecipitated with the anti-FLAG antibody (Fig. 4A), suggesting a very weak interaction between Lrit1 and Lrit3. These results suggested that Lrit1 forms a homodimer and/or a heterodimer with Lrit2. Although I do not exclude the possibility that Lrit1 trans-synaptically interacts with Lrit3 in bipolar dendritic tips, my results suggest that the interaction between Lrit1 and Lrit3 is much weaker than that between Lrit1 and Lrit2.

I then examined the interaction between Elfn1 and Lrit1/2, both of which contain the LRR domains. Lrit1-FLAG or FLAG-tagged Lrit2 (Lrit2-FLAG) was expressed in HEK293 cells with HA-tagged Elfn1 (Elfn1-HA), and immunoprecipitated Lrit1-FLAG or Lrit2-FLAG using the anti-FLAG antibody. I found that Elfn1-HA co-immunoprecipitated with Lrit1-FLAG and Lrit2-FLAG (Fig. 4B). This result suggests that Lrit1 and/or Lrit2 can form a complex with Elfn1 at the rod presynaptic terminal. However, I observed that rod synaptic structure and signal transmission between rods and rod-ON bipolar cells were not affected in either the *Lrit1*$^{gt/gt}$ or *Lrit1/2* DKO retinas (Fig. 3A, S1H, S2K, L, S5E, F, S6A). Therefore, molecular interactions between Lrit1/2 and Elfn1 seem to be dispensable for synapse formation and synaptic transmission between rod photoreceptor and rod ON-bipolar cells.

Many LRRPs trans-synaptically interact with themselves or with other synaptic proteins through their extracellular domains (de Wit et al., 2011). A photoreceptor synaptic LRRP, Elfn1, is known to interact with Grm6 in *trans* and regulates synapse formation between rod photoreceptor and rod ON-bipolar cells (Cao et al., 2015). Since Elfn1 and Lrit1/2 commonly possess FN3 and LRR domains and both are localized at photoreceptor synaptic terminals, I tested the possibility that Lrit1 and/or Lrit2 physically interact with Grm6. I transfected the Lrit1-HA or Lrit2-HA expression plasmids with a FLAG-tagged Grm6 expression plasmid into HEK293 cells, and immunoprecipitated the HEK293 cell lysates with the anti-FLAG antibody. I found that intense bands of Lrit1-HA and Lrit2-HA immunoprecipitated with the anti-FLAG antibody (Fig. 4C). These results suggest that Grm6 physically interacts with Lrit1 and Lrit2. To determine which region of the Lrit1 protein interacts with Grm6, I prepared constructs expressing an N-terminal extracellular portion (Lrit1-NT) or a C-terminal intracellular domain with the transmembrane domain (Lrit1-CT) of Lrit1 (Fig. 4D), and assessed an interaction between these truncated Lrit1 proteins and Grm6. I observed that Grm6 was immunoprecipitated with Lrit1-NT but not with Lrit1-CT (Fig. 4E), suggesting that the Lrit1 N-terminal portion interacts with Grm6.

The PDZ-binding motif of Lrit1 interacts with a scaffold protein, Frmpd2

Lrit1 contains a PDZ-binding motif (-EYFC) in its C-terminal intracellular domain. Synaptic proteins containing PDZ-binding motifs are known to interact with scaffold proteins possessing PDZ domains (Harris and Lim, 2001). To identify an interaction partner binding to the intracellular domain of Lrit1, I performed a yeast-two hybrid screen of a cDNA library prepared from mouse retina using an intracellular domain of Lrit1

(Lrit1-ICD) as the bait. In this screen, I identified three PDZ domain-containing proteins, Frmpd2 (FERM and PDZ domain-containing 2), Sdcbp, and Grip1, interacting with the Lrit1-ICD. I examined expression levels of these three genes in *Otx2* CKO retina using microarray data, and found that only *Frmpd2* expression markedly decreased in *Otx2* CKO retina, suggesting that *Frmpd2* expression is enriched in photoreceptor cells. Frmpd2 is known to be a basolateral protein in epithelial cells (Stenzel et al., 2009) and acts as a scaffold protein in intestinal epithelial cells (Lipinski et al., 2012), however, no *in vivo* function of Frmpd2 has been clarified yet. To corroborate the interaction between Lrit1 and Frmpd2, I performed an immunoprecipitation assay. I transfected a FLAG-tagged Frmpd2 (Frmpd2-FLAG) and Lrit1 expression plasmids into HEK293 cells, and immunoprecipitated using the anti-FLAG antibody. I found that full-length Lrit1 is immunoprecipitated with the anti-FLAG antibody, showing interaction between Lrit1 and Frmpd2 (Fig. 5A). In contrast, the Lrit1 extracellular domain was not immunoprecipitated with the anti-FLAG antibody, indicating that Frmpd2 interacts with the Lrit1 intracellular domain (Fig. 5A). To determine which Frmpd2 domain binds to Lrit1, I generated several deletion constructs of Frmpd2 and carried out yeast two-hybrid assays (Fig. 5B). I found that only the constructs containing the third PDZ domain (PDZ3) of Frmpd2 interacts with the Lrit1 C-terminal region (Fig. 5B).

Frmpd2 localizes to photoreceptor synaptic terminals in an Lrit1-dependent manner

To investigate the tissue distribution of *Frmpd2*, I performed a northern blot analysis. I observed a single 5.7-kb band of *Frmpd2* in the mouse retina, but not in other tissues examined (Fig. S6G). I then carried out *in situ* hybridization analysis using developing and mature mouse retinal sections (Fig. S6H). A weak *Frmpd2* signal was first observed

in the outer nuclear layer (ONL) at P9 and a stronger signal observed at P21, suggesting that time-dependent *Frmpd2* expression correlates with that of Lrit1 and Lrit2. To investigate the subcellular localization of Frmpd2, I raised an antibody against Frmpd2 that recognizes the Frmpd2 C-terminal region. I immunostained retinal sections using this antibody, and found that Frmpd2 signals localize to photoreceptor synaptic terminals both in cone and rod photoreceptors (Fig. 5C). To examine Frmpd2 localization more precisely, I performed 3D-SIM analysis on the 1M mouse retina. Similarly to Lrit1, Frmpd2 localizes to the narrow membrane region just outside of the synaptic ribbon, which is confined between bipolar cell dendritic tips (Fig. 5D). To test whether *Lrit1* loss affects Frmpd2 localization in photoreceptor synapses, I immunostained control and $Lrit1^{gt/gt}$ retinas using anti-Pikachurin and anti-Frmpd2 antibodies. I observed reduced Frmpd2 signals in $Lrit1^{gt/gt}$ rod and cone photoreceptor synapses (Fig. 5E). These results suggest that Lrit1 directly interacts with Frmpd2 to function at photoreceptor synaptic terminals.

Frmpd2 recruits Lrit1 to the actin cytoskeleton at the submembrane

Since Frmpd2 physically interacts with the Lrit1 C-terminal, I examined whether Frmpd2 affects Lrit1 intracellular localization. I expressed Lrit1 and/or FLAG-tagged Frmpd2 in HEK293 cells and carried out an immunostaining analysis. The Frmpd2-FLAG signal was observed at cell boundary in colocalization with the actin cytoskeleton stained with phalloidin (Fig. 5F upper panels, arrowheads). This result is consistent with the previous finding that the FERM domain of Frmpd2 binds to phosphatidylinositol (Stenzel et al., 2009). When only the Lrit1 expression plasmid was transfected into HEK293 cells, Lrit1 localized to the cytosolic granules surrounding nuclei and did not overlap with the actin staining (Fig. 5F, middle panels). In contrast, when both Lrit1 and

Frmpd2-FLAG expression plasmids were transfected into HEK293 cells, I observed colocalization of the Lrit1 signal with the actin cytoskeleton at the submembrane along with Frmpd2-FLAG (Fig. 5F lower panels, arrowheads). These results suggest that Frmpd2 recruits Lrit1 to the submembrane region.

Lrit1-deficient mice exhibit impaired optokinetic responses (OKRs)

To explore the effect of *Lrit1* loss on visual function at an individual level, I measured OKRs, which is a reflexive eye movement observed in response to moving objects (Stahl, 2004). OKRs are divided into initial and late OKRs based on the time range during eye movement (Gellman et al., 1990; Tabata et al., 2010). The initial OKR is a quick eye movement observed in a short period within 500 ms after visually sensing a moving object, while the late OKR is a series of eye movements altering slow tracking and quick resetting to initial eye position within a longer time period (30 s in this study). To characterize the initial OKRs in the $Lrit1^{gt/gt}$ mice, I used visual motion stimuli with a range of spatiotemporal frequencies (Fig. 6A-Q). $Lrit1^{gt/gt}$ mice showed OKRs to a narrower range of spatial and temporal frequencies compared to control mice (Fig. 6C-F). While the optimal spatial frequency (SFo) and optimal temporal frequency (TFo) were not significantly affected between control and $Lrit1^{gt/gt}$ mice (Fig. 6K, L), the peak amplitudes of the responses in $Lrit1^{gt/gt}$ mice significantly decreased (Fig. 6M).

To further characterize the dependence of the late OKRs (OKNs) on the spatiotemporal frequency of the visual stimulus, the mean eye velocity was calculated during the slow phase of nystagmus for each condition. $Lrit1^{gt/gt}$ mice showed OKR responses to the narrower ranges of spatial and temporal frequencies compared to control mice (Fig. 6G-J). The SFo was not significantly different between control and $Lrit1^{gt/gt}$

mice (Fig. 6N). On the other hand, the TFo of the *Lrit1*$^{gt/gt}$ mice was significantly lower compared with control mice (Fig. 6O). The peak amplitudes of the responses significantly decreased (Fig. 6P). The stimulus speeds at the SFo were almost half of those of control mice (Fig. 6Q). These results suggest that visual acuity of *Lrit1*$^{gt/gt}$ mice for moving objects at high speed is impaired. To examine whether *Lrit1* in photoreceptor cells is responsible for the OKR defects observed in *Lrit1*$^{gt/gt}$ mice, I also analyzed OKRs of ON-bipolar cell-specific *Lrit1* CKO mice by crossing *Lrit1*$^{fl/fl}$ mice with the *Grm6-Cre* BAC transgenic mice (Fig. S3A, C). In the both initial and late OKRs, the OKR amplitudes, SFo and TFo were not significantly different between control and *Lrit1* CKO mice (Fig S7A-O). Taken together, these results suggest that the impaired OKR observed in *Lrit1*$^{gt/gt}$ mice results from *Lrit1* loss in photoreceptor cells.

Discussion

Functional role of *Lrit1* in photoreceptor synapse formation

In the current study, I showed evidence that *Lrit1* is required for the formation of synaptic connections between cone photoreceptor axon terminals and cone ON-bipolar cell dendritic terminals. First, *Lrit1* loss caused a significant volume reduction as well as an irregular pattern of cone photoreceptor synaptic terminal structures observed in flat-mount retinal staining with PNA, indicating the critical role of Lrit1 in the morphological formation of cone synaptic terminals. Second, *Lrit1*$^{-/-}$ mice exhibited decreased ERG b-wave amplitudes and prolonged ERG b-wave implicit times under photopic conditions. Third, Lrit1 localizes to a subregion of photoreceptor synaptic terminals near ON-bipolar dendritic tips.

Loss of function of genes involved in photoreceptor synapse formation between photoreceptors and ON-bipolar cells, including *Pikachurin*, *Dystroglycan*, and *Bassoon,* has been reported to produce prolonged photopic ERG b-wave implicit times (Dick et al., 2003; Omori et al., 2012; Sato et al., 2008). The invagination of bipolar cell processes, but not of horizontal cell processes, into photoreceptors is impaired in *Pikachurin*$^{-/-}$ or retina-specific *Dystroglycan* CKO mice. Both bipolar dendrite and horizontal cell process invagination are impaired in *Bassoon*$^{-/-}$ mice. In contrast, invaginations of bipolar dendrites and horizontal cell processes are not significantly affected in *Lrit1*$^{gt/gt}$ mice. These phenotypic differences suggest that *Lrit1* is not required for the invagination of bipolar dendrites and horizontal cell processes into photoreceptor termini. *Lrit1* loss caused a severe diffusion of cone photoreceptor synaptic terminal marker PNA, suggesting that *Lrit1* regulates the proper formation of the axon terminal structures in cone photoreceptors. *Lrit1*-deficient retinas exhibited histological and

electrophysiological defects in the cone ON pathway but not in the rod pathway. Although these phenotypes seem to be caused by *Lrit1* loss in cones, I cannot exclude the possibility that *Lrit1* loss in rods affects these phenotypes. Future analysis using cone-specific *Lrit1* CKO mice may clarify this point.

Mechanism of Lrit1 in interaction of cone terminals with cone ON-bipolar dendrites

My immunoprecipitation assay identified an interaction of Lrit1 with ON-bipolar postsynaptic terminal protein Grm6, implying a possible function of Lrit1 as a physical linker between photoreceptor pre-synapse and ON-bipolar cell post-synapse. Since I observed that punctate Lrit1 signals localize adjacent to the Grm6 signals at bipolar postsynaptic terminals, not all of the Lrit1 protein seems to interact with Grm6 and vice versa. Although Lrit1 is localized to both rod and cone axon terminals, synaptic transmissions and structures between rod photoreceptors and rod ON-bipolar cells were not affected in $Lrit1^{gt/gt}$ mice. Since there is high sequence homology, a similar expression pattern in rod and cone photoreceptors, and adjacent genomic location between Lrit1 and Lrit2, I first speculated a functional redundancy of these two paralogs. However, I did not find a significant phenotypic difference between $Lrit1^{gt/gt}$ and *Lrit1/2* DKO mice, precluding the possibility of functional redundancy between Lrit1 and Lrit2. There is still a possibility that Lrit2 has an essential function in bipolar terminals in the IPL. Elfn1 is known to be enriched in rod photoreceptor synaptic terminals and essential for selective synapse formation between rod photoreceptors and rod ON-bipolar cells through interacting with Grm6 in *trans* (Cao et al., 2015). Domain structures of Lrit1 and Elfn1 are comparatively similar. Both Elfn1 and Lrit1 contain LRR, FN3, and transmembrane domains. In rod photoreceptors, Lrit1 might be involved in synaptic connection formation,

however, Lrit1 is dispensable while Elfn1 is essential. On the other hand, synaptic connections between cone photoreceptors and cone ON-bipolar cells were unaffected in *Elfn1*$^{-/-}$ mice, but synaptic connection between cone photoreceptors and cone ON-bipolar cells was aberrant in *Lrit1*$^{gt/gt}$ retinas. *Lrit1*$^{gt/gt}$ mice exhibited decreased ERG b-wave amplitude under photopic conditions, however, the ERG b-wave was not completely abolished, suggesting that there may be other molecules involved in synapse development between cone photoreceptors and cone ON-bipolar cells. Whereas Lrit3 is essential for proper synaptic transmission in both rod and cone pathways, the defects observed in cone synapses were more severe than those in rod synapses in the *Lrit3* mutant mouse retina (Neuille et al., 2017; Neuille et al., 2015). For example, in the *Lrit3* mutant mouse retina, the Grm6 signal is almost absent in cone bipolar dendritic tips but unaffected in rod bipolar dendritic tips. Cone-dominant phenotypes observed in both *Lrit1* and *Lrit3* mutant retinas raise the possibility of a direct trans-synaptic interaction between Lrit1 and Lrit3 proteins in cone synapses. However, in the immunoprecipitation assay, I observed only a very faint band of Lrit3 immunoprecipitated by Lrit1 (Fig. 4A). In addition, Lrit3 localization was not affected in the *Lrit1*$^{gt/gt}$ retina (Fig. S1H). Based on these results, Lrit1 seems to function in a different molecular pathway than Lrit3.

Functional mechanism of Lrit1 in cone photoreceptor terminals

Cone photoreceptor terminals exhibited an aberrant morphology that may reduce synaptic transmission efficiency between cone photoreceptors and cone ON-bipolar cells. How does *Lrit1* loss affect cone photoreceptor terminals? In the current study, I identified a FERM domain-containing scaffold protein, Frmpd2, which interacts with Lrit1. Frmpd2 was previously reported to localize to the basolateral membrane in epithelial cells through

binding to phosphatidylinositol (Stenzel et al., 2009). This studies showed that mouse *Frmpd2* is enriched in the retina and that the C-terminal intercellular domain of Lrit1 interacts with the third PDZ domain of Frmpd2, suggesting a mechanism in which Lrit1 is anchored in the submembrane region of photoreceptor synaptic terminals through interaction with Frmpd2. In HEK293 cells Lrit1 becomes colocalized to the submembrarne region upon Frmpd2 expression, while Frmpd2 is diffuse in the *Lrit1*-null retina (Fig. 5E). These results suggest that Lrit1 and Frmpd2 directly interact at photoreceptor synaptic terminals in an interdependent manner. Frmpd2 is known to act as a membrane scaffolding protein in intestinal epithelial cells (Lipinski et al., 2012). Taken together, these observations suggest that Frmpd2 regulates the formation and stabilization of photoreceptor axon terminal structures by acting as a scaffolding protein.

In the current study, my 3D-SIM analysis confirmed that Lrit1 localizes to the small areas of photoreceptor terminals wedged between two dendritic tips of the ON-bipolar cell. Frmpd2 also localizes to the same subregion of photoreceptor synaptic terminals. Interestingly, to my best knowledge no protein has been reported to localize to this subregion of the photoreceptor axon terminal. Further study of photoreceptor-bipolar synapse formation may further my understanding of the significance of the subregion where the Lrit1-Frmpd2 complex localizes.

As a whole, my results suggest that Lrit1 regulates cone photoreceptor-ON cone bipolar synapse development through the Frmpd2-Lrit1-Grm6 axis (Fig. S7P).

The role of the cone photoreceptor-cone ON bipolar pathway in visual function

It was previously studied the OKR of mutant mice with ON bipolar cell dysfunction (*Trpm1*$^{-/-}$ and *Grm6*$^{-/-}$) (Sugita et al., 2013). These mutant mice showed significantly

smaller amplitudes compared with those of WT control mice in the initial OKR and they showed no activity in the late OKR, suggesting that the initial OKR is mediated by both ON and OFF pathways and the late OKR is mediated solely by the ON-pathway (Sugita et al., 2013). The *Lrit1*$^{gt/gt}$ mice showed smaller amplitudes compared with control mice in initial and late OKRs, suggesting that the ON-pathway is partially impaired in *Lrit1*$^{gt/gt}$ mice. This may reflect that only the cone photoreceptor-cone ON bipolar synapse is specifically impaired in *Lrit1*$^{gt/gt}$ mice but not the rod-photoreceptor-rod ON-bipolar synapse. I observed decreased temporal frequency but normal spatial frequency of late OKR in the *Lrit1*$^{gt/gt}$ mice. This implies the possibility that the Lrit1-mediated cone photoreceptor-cone ON-bipolar pathway is required for temporal sensitivity, but not for spatial sensitivity in vision.

Materials and Methods

Animal care

All procedures conformed to the ARVO statement for the Use of Animals in Ophthalmic and Vision Research. These procedures were approved by the Institutional Safety Committee on Recombinant DNA Experiments (approval ID 04220) and Animal Experimental Committees of the Institute for Protein Research (approval ID 29-01-0) at Osaka University, and were performed in compliance with the institutional guidelines. Mice were housed in a temperature-controlled room at 22°C with a 12h light/dark cycle. Fresh water and rodent diet were available at all times. All animal experiments were performed with mice of either sex.

Generation of *Lrit1*$^{gt/gt}$ mice

I generated *Lrit1*$^{gt/gt}$ mice as follows: *Lrit1*$^{gt/gt}$ ES cells (*Lrit1*$^{tm1a(EUCOMM)Hmgu}$; ES cell clone HEPD0832_7_G03; parental ES cell line JM8.N4) obtained from the European Conditional Mouse Mutagenesis Program (EUCOMM) were injected into ICR blastocysts to obtain chimeric mice. *Lrit1*$^{gt/+}$ mice were generated by crossing chimeric mice with C57BL/6J mice and crossing the resulting generations with each other to obtain *Lrit1*$^{gt/gt}$ mice.

Generation of *Lrit1* CKO mice

Lrit1$^{fl/fl}$ mice were generated by crossing *Lrit1*$^{gt/gt}$ mice with B6-Tg(*CAG-FLPe*)37 mice (RIKEN BRC, #RBRC01835) (Kanki et al., 2006). *Lrit1* CKO mice were generated by crossing *Lrit1*$^{fl/fl}$ mouse line with the *Grm6-Cre* transgenic mouse line, which I generated

by expressing Cre recombinase driven by the 9.5 kb *Grm6* promoter (RIKEN BRC, #RBRC05744). The *Grm6-Cre-pA* transgene was purified as described previously (Sato et al., 2007). This purified construct was injected into the pronuclei of fertilized one-cell eggs of B6C3F1 mice. To observe Cre recombinase activities in the *Grm6-Cre* transgenic mice, I crossed them with a *R26-CAG-LoxP-mTFP1* reporter strain (RIKEN BRC, #RBRC05147) (Imayoshi et al., 2012). *Grm6-Cre:R26-CAG-LoxP-mTFP1* mice were then analyzed for mTFP1 expression.

Generation of *Lrit1/2* DKO mice

I obtained *Lrit1* and *Lrit2* genomic clones by PCR using a JM8A3 mouse genome as a template. I subcloned a 4.8 kb NotI-BamHI fragment from the *Lrit1* and a 4.9 kb ClaI-ClaI fragment from the *Lrit2* genomic loci into a modified pPNT vector (Deng et al., 1996) to generate a targeting construct, and transfected the linearized targeting construct into the JM8A3 (C57BL/6N) embryonic stem (ES) cells. The culture, electroporation, and selection of ES cells were carried out as previously described (Muranishi et al., 2011). ES cells that were heterozygous for the targeted gene disruption were microinjected into C57BL/6 blastocysts to obtain chimeric mice.

Generation of *Lrit2*$^{-/-}$ mice

Lrit2$^{-/-}$ mice were generated using the CRISPR/Cas9 system. The gRNA was designed within exon 2 of the *Lrit2* gene using CRISPR Design (http://crispr.mit.edu/). The oligo DNAs for the gRNA sequence were cloned into the pX330 vector (Cong et al., 2013). *Cas9* mRNA and *Lrit2* gRNA were synthesized and purified using the MEGAshortscript^{TM} T7 Transcription Kit (Ambion) and mMESSAGE mMACHINE T7

Ultra Kit (Ambion), respectively. *Cas9* mRNA (100 ng/μl) and *Lrit2* gRNA (8 ng/μl) were co-injected in the pronucleus of BDF1 fertilized eggs in mWM medium and were transferred into the uterus of pseudopregnant ICR females. Mutated individuals were selected by PCR and sequence analysis.

In situ hybridization

In situ hybridization was performed as described previously (Omori et al., 2010). Mouse eye cups at P3, P9, and P21 were fixed using 4% PFA in PBS overnight at room temperature. Digoxigenin-labeled riboprobes for mouse *Lrit1*, *Lrit2,* and *Frmpd2* were synthesized by *in vitro* transcription using 11-digoxigenin UTPs (Roche). *Lrit1, Lrit2,* and *Frmpd2* cDNA fragments for *in situ* hybridization probes were generated by RT-PCR using mouse retinal cDNA as templates. The sequences of primers used are described in Table 1

Northern blot analysis

Northern blot analysis was performed as described previously (Chaya et al., 2014). Total RNAs were extracted using TRIzol (Ambion) from tissues dissected from P28 ICR mice. 10μg of total RNA was electrophoresed on a 1.0% agarose formaldehyde gel and transferred to a nylon membrane (Pall). The same regions of *Lrit1*, *Lrit2*, and *Frmpd2* cDNAs used for the *in situ* hybridization probes were used to synthesize radiolabeled probes. The cDNA probes were labeled with ^{32}P-dCTP using the Rediprime II random prime labeling system (GE Healthcare). Primers used for amplification of *Lrit1*, *Lrit2*, and *Frmpd2* cDNA fragments for the probes were listed in Table 1.

Immunofluorescent analysis of retinal sections and cells

Immunohistochemical analysis of retinal sections was performed as described previously (Omori et al., 2010). Mouse eye cups were fixed by 4% PFA in PBS for 30 min at room temperature. The retinas were rinsed in PBS and cryoprotected with 30% sucrose in PBS overnight at 4°C. The samples were embedded in TissueTec OCT compound 4583 (Sakura), frozen, and sectioned. Frozen 20 μm sections on slides were dried for 2 hr at room temperature, rehydrated in PBS for 5 min, incubated with blocking buffer (5% normal donkey serum, and 0.1% Triton X-100 in PBS) for 1 hr, and then with primary antibodies for 4 hr at room temperature or overnight at 4°C. Slides were washed with PBS three times for 5 min each time and incubated with fluorescent dye-conjugated secondary antibodies and DAPI (1:1000, Nacalai Tesque) for 2 hr at room temperature with shielded from light. The sections were coverslipped with gelvatol after being washed with PBS.

For flat-mount immunostaining of retina, each retina was gently peeled off from the sclera, rinsed in PBS and fixed with 4% PFA in PBS for 30 min at room temperature. The lenses were removed after wash. The retinas were incubated with blocking buffer for 1 hr, and then with the anti-Arrestin3 antibody (Millipore AB15282, 1:500) overnight at 4°C. Samples were washed with PBS three times and incubated with fluorescent dye-conjugated secondary antibodies and/or rhodamine-labeled PNA (Vector Laboratories, 1:250) for 2 hr at room temperature. After three PBS washes, the samples were permeabilized by incubation in gelvatol for 5 min. The specimens were observed under a laser confocal microscope (LSM700, Carl Zeiss). Quantification of the Arrestin3-stained cone pedicle area was performed by MetaMorph software (WT; n=3, *Lrit1*$^{gt/gt}$; n=4, 45 pedicles from each animal). Morphological classification of cone synapse clusters was performed by Photoshop and ImageJ software using maximum projection images (512 x

512 pixels) captured by confocal microscopy using 40x lens. Morphological definitions are as follows: Diffused, clusters whose morphological features are unrecognizable at a threshold value of 55; Fused, clusters in contact with one or more other clusters; Shrunken, clusters whose short axes are less than 50% of normal clusters (16 pixels) in WT (WT; n=3, *Lrit1*$^{gt/gt}$; n=3 for Figure 2D, WT; n=3, *Lrit1/2 DKO*; n=4 for Figure S5D). To generate X-Y coordinates for Voronoi domain analysis, the center of each pedicle was marked manually on maximum projection images (512 x 512 pixels) captured by confocal microscopy using a 40x lens and Photoshop software. Voronoi domain areas were analyzed using ImageJ software (WT; n=3, *Lrit1*$^{gt/gt}$; n=3). To calculate the Voronoi domain regularity index, the mean of Voronoi domain areas for a given cone pedicle array was divided by a standard deviation of the analyzed areas.

HEK293 cells were cultured in DMEM (Sigma) with 10% fetal bovine serum. At 48 hr post-transfection, cells were fixed with 4% PFA in PBS for 10 min at room temperature and immunostained as described for tissue sections. Primary antibodies used in this study are described as follows: mouse anti-Ctbp2 (1:500, BD Biosciences), rabbit anti-Pikachurin (1:300) (Sato et al., 2008), rabbit anti-Trpm1 (1:100) (Koike et al., 2010b), rabbit anti-Dystroglycan H-242 (1:300, Santa Cruz Biotechnology), rabbit anti-Elfn1 (1:500, a kind gift from Dr. Martemyanov KA) (Cao et al., 2015), guinea pig anti-Frmpd2 (1:500, current study), mouse anti-FLAG M2(1:1000, Sigma), guinea pig anti-Grm6 (1:3000) (Koike et al., 2010b), mouse anti-Znp1 (1:500, ZIRC), rabbit anti-Calbindin-D28K (1:500, Calbiochem), rabbit anti-PKCα (1:500, Sigma), guinea pig anti-Lrit1 (1:500, current study). Cy3-conjugated (1:500, Jackson ImmunoResearch Laboratories), Alexa Fluor 488-conjugated (1:500, Sigma) or Dylight649-conjugated secondary antibodies (1:500, Jackson ImmunoResearch Laboratories) were used. AF488-conjugated

Phalloidin (1:500, Invitrogen) was used for staining F-actin. For pre-absorption of the anti-Frmpd2 antibody with its antigen, the anti-Frmpd2 antibody was incubated with 8 μg of the purified His-tagged residues 1151-1272 of the Frmpd2 protein overnight at 4°C in 500 μl of blocking buffer. Frmpd2 signals in the OPL of the 1M mouse retina were observed with the anti-Frmpd2 antibody, but were absent with the pre-absorbed antibody.

Immunoprecipitation Assay

Immunoprecipitation assay was performed as described previously (Omori et al., 2010). HEK293 cells were co-transfected with FLAG-tagged protein expression plasmids and other expression plasmids using calcium phosphate buffer (140 mM NaCl, 125 mM $CaCl_2$, 25 mM BES (pH 6.98), and 0.75 mM Na_2HPO_4). At 48 hr after transfection, the cells were lysed in a lysis buffer (1% Triton X-100 in PBS) supplemented with protease inhibitors (1 mM PMSF, 2 μg/ml leupeptin, 5 μg/ml aprotinin, and 3 μg/ml pepstatin A), and centrifuged for 10 min at 15,000rpm. An anti-FLAG M2 affinity gel (Invitrogen) was used for immunoprecipitation of FLAG-fusion proteins. The supernatants were incubated with anti-FLAG M2 affinity gel overnight at 4°C and washed 5 times with wash buffer (1% Triton X-100 in PBS). The beads were incubated with SDS-sample buffer for 30 min at room temperature.

Western blot analysis

Western blot analysis was performed as described previously (Chaya et al., 2014). Samples were resolved by SDS-PAGE and transferred to PVDF membranes (Millipore) using a semidry transfer cell (Bio-Rad). The membranes were blocked with blocking buffer (5% skim milk (W/V), and 0.1% Tween 20 in TBS) and incubated with primary

antibodies overnight at 4°C. The membranes were washed with 0.1% Tween20 in TBS three times for 10 min each time, and then incubated with secondary antibodies for 2 hr at room temperature. Signals were detected using Chemi-Lumi One L (Nacalai, Japan) or Pierce Western Blotting Substrate Plus (Thermo Fisher Scientific). I used the following primary antibodies: mouse anti-FLAG M2 (1:6000, Sigma), rat anti-HA (1:5000, Santa Cruz), and guinea pig anti-Lrit1 (1:1000, generated in this study) antibodies. The following secondary antibodies were used: horseradish peroxidase-conjugated anti-mouse IgG (1:10,000, Zymed), anti-guinea pig IgG (1:10,000, Jackson Laboratory), and anti-rabbit IgG (1:10,000, Jackson Laboratory).

Plasmid constructs

To generate the pGrm6-Cre-pA plasmid, I subcloned a 9.5-kb mouse *Grm6* promoter (Ueda et al., 1997) into a modified pβ-gal-Basic vector (Clontech) in which the β-gal gene was swapped for a Cre gene. To construct the plasmids expressing full-length Lrit1, FLAG-tagged full-length Lrit1, HA-tagged full-length Lrit1, or FLAG-tagged Lrit1 extracellular domain, a cDNA fragment encoding full-length Lrit1 (residues 1-624) or the extracellular domain (residues 1-528) of Lrit1 was amplified by PCR using mouse retinal cDNA as a template and cloned into the pCAGGSII expression vector. The Lrit1-NT and -CT truncated mutations were introduced by site-directed mutagenesis by PCR, and ligated into the C-terminal FLAG-tagged pCAGGSII expression vectors. A cDNA fragment encoding full length mouse Frmpd2 (residues 1-1292) was amplified by PCR, and ligated into the C-terminal FLAG-tagged pCAGGSII expression vector to generate pCAGGSII-FLAG-Frmpd2. A cDNA encoding full length mouse Grm6 (residues 1-871) or Lrit2 (residues 1-549) was amplified from mouse retinal cDNA by PCR, then

subcloned into the C-terminal HA-tagged pCAGGSII plasmid.

ERG recording

The method of recording the electroretinograms (ERGs) was performed as described previously with some modifications (Omori et al., 2015). In brief, one-month-old mice were dark adapted for more than 4 hr, and then anesthetized with an intraperitoneal injection of 100mg/kg ketamine and 10mg/kg xylazine. ERG responses were measured using the PuREC system with LED electrodes (Mayo Corporation). The mice were placed on a heating pad and stimulated with four levels of stroboscopic stimuli ranging from -4.0 to 1.0 log cd sm^{-2} to elicit scotopic ERG. After mice were light adapted for 10 min, the photopic ERGs were recorded on a rod-suppressing white background of 1.3 log cd sm^{-2}. Four levels of stimulus intensities ranging from -0.5 to 1 log cd sm^{-2} were used for the photopic ERG recordings. Eight responses were averaged for scotopic recordings (-4.0 and -3.0 log cd sm^{-2}). Sixteen responses were averaged for photopic recordings.

Intravitreal drug administration

Intravitreal injection was performed using a protocol described previously with modifications (Sharma et al., 2005; Shirato et al., 2008). A small hole was created with a 30-gauge needle 500 μm posterior to the limbus, and 1.5 μl of the solution was injected into the eye through a micro syringe (Ito Corporation) with a 33-gauge blunt-ended needle. APB (L-AP4, Sigma-Aldrich) was utilized to block the ON pathway (Sharma et al., 2005; Shirato et al., 2008). The vitreal concentration of L-AP4 was designed to be 2 mM. I recorded an ERG after injection.

RT-PCR

Total retinal RNA was isolated using Trizol reagent (Thermo Fisher Scientific), and reverse transcribed into cDNA using SuperScript II Reverse Transcriptase (Thermo Fisher Scientific) with random hexamers and oligo (dT) $_{12\text{-}18}$ primers. The cDNAs were amplified by PCR using rTaq polymerase (TaKaRa). Primers used for amplification of *Lrit1*, *Lrit2,* and *β-actin* are listed in Table 1.

Transmission Electron Microscope

Mouse eye cups were fixed with 2% glutaraldehyde and 2% PFA for 2 hr. After fixation with 1% osmium tetroxide for 90 min, the retinas were dehydrated through a graded series of ethanol (50-100%) and cleared by propylene oxide. The retinas were embedded in epoxy resin. Ultrathin sections were cut on an ultramicrotome (Ultracut E; Reichert-Jung), and stained with uranyl acetate and lead citrate. Retinas were observed by transmission electron microscope (H-7650; Hitachi Co)

Antibody production

cDNA fragments encoding a middle portion of mouse Lrit1 (residues 337-430) and Frmpd2 (residues 1151-1272) were amplified by PCR using the RIKEN full-length enriched library as templates and subcloned into pGEX4T-1 plasmid (GE Healthcare) and pET28b plasmid respectively. The GST-Lrit1 fusion protein or His-Frmpd2 fusion protein was expressed in *Escherichia coli* strain BL21 and purified with glutathione Sepharose 4B (GE Healthcare) or Ni-NTA agarose (Qiagen) according to the manufacturer's instructions. The anti-Lrit1 and anti-Frmpd2 antibodies were obtained by immunizing guinea pigs with the purified GST-Lrit1 or His-Frmpd2.

Yeast two-hybrid assays

I carried out a yeast two-hybrid screen using MATCHMAKER GAL4 Two-Hybrid System3 (TaKaRa Bio). A cDNA fragment encoding the intracellular domain of mouse *Lrit1* (residues 529-624) was inserted into the pGBKT7 bait plasmid and transformed into the AH109 yeast strain. I screened 1.0 x 10^6 transformants from a mouse developing and adult retinal cDNA library which I generated. A total of 32 positive colonies were identified on the basis of their ability to express the nutritional markers ADE2 and HIS3 by plating on SD-Trp-Leu-Ade-His media. Thirty colonies were positive in the β-galactosidase (β-gal) assay. The plasmids were isolated from yeast using Zymoprep™ Yeast Plasmid Miniprep I (The Epigenetics Company) and transformed into E. coli DH5α. Fifteen clones were obtained, and ultimately I identified 13 genes encoding proteins that interact with Lrit1.

To identify the Lrit1-interacting domains of Frmpd2, a cDNA encoding a full length Frmpd2 (residues 1-1292) or deletion mutants (KIND+FERM: 1-753, PDZ1: 753-910, PDZ2: 911-1055, PDZ3: 1052-1292) was cloned into the pGADT7 prey vector and transformed into the AH109 yeast strain bearing the bait plasmid pGBKT7-Lrit1 (residues 529-624). The ability to express markers (ADE2, HIS3, and LacZ) was investigated by nutritional selection and β-gal assay.

3D-SIM analysis

The retinal photoreceptor synapses in the OPL were observed with super-resolution microscopy based on confocal microscope optics (Hayashi and Okada, 2015). The raw images were taken with the objective lens, HCPLAPO100x/1.40 Oil on a SP-8 confocal

microscope (Leica). The pinhole was reduced to a size corresponding to 0.5 Airy units at 580 nm. Three dimensional twice oversampled data were further processed by the classical maximum likelihood estimation deconvolution algorithm (Huygens, Scientific Volume Imaging) to enhance the high resolution components beyond the classical diffraction limit of 200 nm. The three-dimensional (3D) views of the photoreceptor synapses were reconstructed from serial images (Z-stack) obtained by super-resolution imaging. The quantification of PNA signal volumes was performed using Image J software.

OKR recording

OKR recording was performed as previously described (Sugita et al., 2015; Sugita et al., 2013; Tabata et al., 2010; Watanabe et al., 2015). The mouse right eye was illuminated by infrared light emitting diodes and monitored with a CCD camera using image- processing software (Geteye, Matsuura-Denko-sha). The visual stimuli were moving sinusoidal gratings with one of five spatial frequencies selected randomly from a lookup table: 0.0313, 0.0625, 0.125, 0.25, and 0.5 cycle/deg in a given trial. The temporal frequency was selected from 0.1875, 0.375, 0.75, 1.5, 3, 6, 12, or 24 Hz. Techniques for the eye movement recording and visual stimulation were similar to those described in previous studies (Sugita et al., 2015; Sugita et al., 2013; Tabata et al., 2010; Watanabe et al., 2015). In the initial OKR experiment, the data on six WT control and seven *Lrit1*$^{gt/gt}$ mice, and six *Grm6-Cre* control and five *Lrit1* CKO mice were obtained. In the late OKR experiment, the data on eight WT control and eight *Lrit1*$^{gt/gt}$ mice, and six *Grm6-Cre* control and five *Lrit1* CKO mice were obtained. I used a sinusoidal grating pattern with a contrast and mean luminance of 64% and 100 cd/m^2, respectively (Sugita et al., 2015;

Sugita et al., 2013; Tabata et al., 2010). Amplitude of initial OKRs was defined as the mean eye velocity during the 100-ms interval starting 100-ms after the onset of visual motion. Amplitude of late OKRs (OKN) was defined as the mean eye velocity during the 20-s interval starting 10-ms after the onset of visual motion.

Statistical analysis

Statistical analysis was performed using Student`s *t*-test, and $p < 0.05$ was taken to be statistically significant. Data are expressed as mean ± SD.

References

Bassett, E.A., and Wallace, V.A. (2012). Cell fate determination in the vertebrate retina. Trends Neurosci *35*, 565-573.

Behnia, R., Clark, D.A., Carter, A.G., Clandinin, T.R., and Desplan, C. (2014). Processing properties of ON and OFF pathways for Drosophila motion detection. Nature *512*, 427-430.
Bella, J., Hindle, K.L., McEwan, P.A., and Lovell, S.C. (2008). The leucine-rich repeat structure. Cell Mol Life Sci *65*, 2307-2333.

Blanks, J.C., Adinolfi, A.M., and Lolley, R.N. (1974). Synaptogenesis in the photoreceptor terminal of the mouse retina. J Comp Neurol *156*, 81-93.

Cao, Y., Sarria, I., Fehlhaber, K.E., Kamasawa, N., Orlandi, C., James, K.N., Hazen, J.L., Gardner, M.R., Farzan, M., Lee, A.*, et al.* (2015). Mechanism for Selective Synaptic Wiring of Rod Photoreceptors into the Retinal Circuitry and Its Role in Vision. Neuron *87*, 1248-1260.

Chaya, T., Matsumoto, A., Sugita, Y., Watanabe, S., Kuwahara, R., Tachibana, M., and Furukawa, T. (2017). Versatile functional roles of horizontal cells in the retinal circuit. Sci Rep *7*, 5540.

Chaya, T., Omori, Y., Kuwahara, R., and Furukawa, T. (2014). ICK is essential for cell type-specific ciliogenesis and the regulation of ciliary transport. EMBO J *33*, 1227-1242.

Condomitti, G., Wierda, K.D., Schroeder, A., Rubio, S.E., Vennekens, K.M., Orlandi, C., Martemyanov, K.A., Gounko, N.V., Savas, J.N., and de Wit, J. (2018). An Input-Specific Orphan Receptor GPR158-HSPG Interaction Organizes Hippocampal Mossy Fiber-CA3 Synapses. Neuron *100*, 201-215 e209.

Cong, L., Ran, F.A., Cox, D., Lin, S., Barretto, R., Habib, N., Hsu, P.D., Wu, X., Jiang, W., Marraffini, L.A.*, et al.* (2013). Multiplex genome engineering using CRISPR/Cas systems. Science *339*, 819-823.

D'Orazi, F.D., Suzuki, S.C., and Wong, R.O. (2014). Neuronal remodeling in retinal circuit assembly, disassembly, and reassembly. Trends Neurosci *37*, 594-603.

Dalva, M.B., Takasu, M.A., Lin, M.Z., Shamah, S.M., Hu, L., Gale, N.W., and Greenberg, M.E. (2000). EphB receptors interact with NMDA receptors and regulate excitatory synapse formation. Cell *103*, 945-956.

de Wit, J., Hong, W., Luo, L., and Ghosh, A. (2011). Role of leucine-rich repeat proteins in the development and function of neural circuits. Annu Rev Cell Dev Biol *27*, 697-729.

Deng, C., Wynshaw-Boris, A., Zhou, F., Kuo, A., and Leder, P. (1996). Fibroblast growth factor receptor 3 is a negative regulator of bone growth. Cell *84*, 911-921.

Dick, O., tom Dieck, S., Altrock, W.D., Ammermuller, J., Weiler, R., Garner, C.C., Gundelfinger, E.D., and Brandstatter, J.H. (2003). The presynaptic active zone protein bassoon is essential for photoreceptor ribbon synapse formation in the retina. Neuron *37*, 775-786.

Dolan, J., Walshe, K., Alsbury, S., Hokamp, K., O'Keeffe, S., Okafuji, T., Miller, S.F., Tear, G., and Mitchell, K.J. (2007). The extracellular leucine-rich repeat superfamily; a comparative survey and analysis of evolutionary relationships and expression patterns. BMC Genomics *8*, 320.

Furukawa, T., Ueno, A., and Omori, Y. (2019). Molecular mechanisms underlying selective synapse formation of vertebrate retinal photoreceptor cells. Cell Mol Life Sci.

Gellman, R.S., Carl, J.R., and Miles, F.A. (1990). Short latency ocular-following responses in man. Vis Neurosci *5*, 107-122.

Gomi, F., Imaizumi, K., Yoneda, T., Taniguchi, M., Mori, Y., Miyoshi, K., Hitomi, J., Fujikado, T., Tano, Y., and Tohyama, M. (2000). Molecular cloning of a novel membrane glycoprotein, pal, specifically expressed in photoreceptor cells of the retina and containing leucine-rich repeat. J Neurosci *20*, 3206-3213.

Harris, B.Z., and Lim, W.A. (2001). Mechanism and role of PDZ domains in signaling complex assembly. J Cell Sci *114*, 3219-3231.

Hayashi, S., and Okada, Y. (2015). Ultrafast superresolution fluorescence imaging with

spinning disk confocal microscope optics. Mol Biol Cell *26*, 1743-1751.

Heidelberger, R., Thoreson, W.B., and Witkovsky, P. (2005). Synaptic transmission at retinal ribbon synapses. Prog Retin Eye Res *24*, 682-720.

Herrmann, R., Heflin, S.J., Hammond, T., Lee, B., Wang, J., Gainetdinov, R.R., Caron, M.G., Eggers, E.D., Frishman, L.J., McCall, M.A.*, et al.* (2011). Rod vision is controlled by dopamine-dependent sensitization of rod bipolar cells by GABA. Neuron *72*, 101-110.

Imayoshi, I., Hirano, K., Sakamoto, M., Miyoshi, G., Imura, T., Kitano, S., Miyachi, H., and Kageyama, R. (2012). A multifunctional teal-fluorescent Rosa26 reporter mouse line for Cre- and Flp-mediated recombination. Neurosci Res *73*, 85-91.

Jin, M.S., Kim, S.E., Heo, J.Y., Lee, M.E., Kim, H.M., Paik, S.G., Lee, H., and Lee, J.O. (2007). Crystal structure of the TLR1-TLR2 heterodimer induced by binding of a tri-acylated lipopeptide. Cell *130*, 1071-1082.

Kanagawa, M., Omori, Y., Sato, S., Kobayashi, K., Miyagoe-Suzuki, Y., Takeda, S., Endo, T., Furukawa, T., and Toda, T. (2010). Post-translational maturation of dystroglycan is necessary for pikachurin binding and ribbon synaptic localization. J Biol Chem *285*, 31208-31216.

Kanki, H., Suzuki, H., and Itohara, S. (2006). High-efficiency CAG-FLPe deleter mice in C57BL/6J background. Exp Anim *55*, 137-141.

Kay, J.N., Chu, M.W., and Sanes, J.R. (2012). MEGF10 and MEGF11 mediate homotypic interactions required for mosaic spacing of retinal neurons. Nature *483*, 465-469.

Keeley, P.W., Luna, G., Fariss, R.N., Skyles, K.A., Madsen, N.R., Raven, M.A., Poche, R.A., Swindell, E.C., Jamrich, M., Oh, E.C.*, et al.* (2013). Development and plasticity of outer retinal circuitry following genetic removal of horizontal cells. J Neurosci *33*, 17847-17862.

Kefalov, V.J. (2012). Rod and cone visual pigments and phototransduction through pharmacological, genetic, and physiological approaches. J Biol Chem *287*, 1635-1641.

Koike, C., Numata, T., Ueda, H., Mori, Y., and Furukawa, T. (2010a). TRPM1: a vertebrate TRP channel responsible for retinal ON bipolar function. Cell Calcium *48*, 95-101.

Koike, C., Obara, T., Uriu, Y., Numata, T., Sanuki, R., Miyata, K., Koyasu, T., Ueno, S., Funabiki, K., Tani, A.*, et al.* (2010b). TRPM1 is a component of the retinal ON bipolar cell transduction channel in the mGluR6 cascade. Proc Natl Acad Sci U S A *107*, 332-337.

Korenbrot, J.I. (2012). Speed, sensitivity, and stability of the light response in rod and cone photoreceptors: facts and models. Prog Retin Eye Res *31*, 442-466.

Lipinski, S., Grabe, N., Jacobs, G., Billmann-Born, S., Till, A., Hasler, R., Aden, K., Paulsen, M., Arlt, A., Kraemer, L.*, et al.* (2012). RNAi screening identifies mediators of NOD2 signaling: implications for spatial specificity of MDP recognition. Proc Natl Acad Sci U S A *109*, 21426-21431.

Masland, R.H. (2001). The fundamental plan of the retina. Nat Neurosci *4*, 877-886.

Matsuda, K., Miura, E., Miyazaki, T., Kakegawa, W., Emi, K., Narumi, S., Fukazawa, Y., Ito-Ishida, A., Kondo, T., Shigemoto, R.*, et al.* (2010). Cbln1 is a ligand for an orphan glutamate receptor delta2, a bidirectional synapse organizer. Science *328*, 363-368.

Matthews, G., and Fuchs, P. (2010). The diverse roles of ribbon synapses in sensory neurotransmission. Nat Rev Neurosci *11*, 812-822.

Morigiwa, K., and Vardi, N. (1999). Differential expression of ionotropic glutamate receptor subunits in the outer retina. J Comp Neurol *405*, 173-184.

Muranishi, Y., Terada, K., Inoue, T., Katoh, K., Tsujii, T., Sanuki, R., Kurokawa, D., Aizawa, S., Tamaki, Y., and Furukawa, T. (2011). An essential role for RAX homeoprotein and NOTCH-HES signaling in Otx2 expression in embryonic retinal photoreceptor cell fate determination. J Neurosci *31*, 16792-16807.

Nakanishi, S., Nakajima, Y., Masu, M., Ueda, Y., Nakahara, K., Watanabe, D., Yamaguchi, S., Kawabata, S., and Okada, M. (1998). Glutamate receptors: brain function and signal transduction. Brain Res Brain Res Rev *26*, 230-235.

Neuille, M., Cao, Y., Caplette, R., Guerrero-Given, D., Thomas, C., Kamasawa, N., Sahel, J.A., Hamel, C.P., Audo, I., Picaud, S.*, et al.* (2017). LRIT3 Differentially Affects Connectivity and

Synaptic Transmission of Cones to ON- and OFF-Bipolar Cells. Invest Ophthalmol Vis Sci *58*, 1768-1778.

Neuille, M., Morgans, C.W., Cao, Y., Orhan, E., Michiels, C., Sahel, J.A., Audo, I., Duvoisin, R.M., Martemyanov, K.A., and Zeitz, C. (2015). LRIT3 is essential to localize TRPM1 to the dendritic tips of depolarizing bipolar cells and may play a role in cone synapse formation. Eur J Neurosci *42*, 1966-1975.

Nishida, A., Furukawa, A., Koike, C., Tano, Y., Aizawa, S., Matsuo, I., and Furukawa, T. (2003). Otx2 homeobox gene controls retinal photoreceptor cell fate and pineal gland development. Nat Neurosci *6*, 1255-1263.

Omori, Y., Araki, F., Chaya, T., Kajimura, N., Irie, S., Terada, K., Muranishi, Y., Tsujii, T., Ueno, S., Koyasu, T.*, et al.* (2012). Presynaptic dystroglycan-pikachurin complex regulates the proper synaptic connection between retinal photoreceptor and bipolar cells. J Neurosci *32*, 6126-6137.

Omori, Y., Chaya, T., Katoh, K., Kajimura, N., Sato, S., Muraoka, K., Ueno, S., Koyasu, T., Kondo, M., and Furukawa, T. (2010). Negative regulation of ciliary length by ciliary male germ cell-associated kinase (Mak) is required for retinal photoreceptor survival. Proc Natl Acad Sci U S A *107*, 22671-22676.

Omori, Y., Katoh, K., Sato, S., Muranishi, Y., Chaya, T., Onishi, A., Minami, T., Fujikado, T., and Furukawa, T. (2011). Analysis of transcriptional regulatory pathways of photoreceptor genes by expression profiling of the Otx2-deficient retina. PLoS One *6*, e19685.

Omori, Y., Kitamura, T., Yoshida, S., Kuwahara, R., Chaya, T., Irie, S., and Furukawa, T. (2015). Mef2d is essential for the maturation and integrity of retinal photoreceptor and bipolar cells. Genes Cells *20*, 408-426.

Orlandi, C., Omori, Y., Wang, Y., Cao, Y., Ueno, A., Roux, M.J., Condomitti, G., de Wit, J., Kanagawa, M., Furukawa, T.*, et al.* (2018). Transsynaptic Binding of Orphan Receptor GPR179 to Dystroglycan-Pikachurin Complex Is Essential for the Synaptic Organization of Photoreceptors. Cell Rep *25*, 130-145 e135.

Parsons, T.D., and Sterling, P. (2003). Synaptic ribbon. Conveyor belt or safety belt? Neuron

37, 379-382.

Penzes, P., Cahill, M.E., Jones, K.A., VanLeeuwen, J.E., and Woolfrey, K.M. (2011). Dendritic spine pathology in neuropsychiatric disorders. Nat Neurosci *14*, 285-293.

Rich, K.A., Zhan, Y., and Blanks, J.C. (1997). Migration and synaptogenesis of cone photoreceptors in the developing mouse retina. J Comp Neurol *388*, 47-63.

Robbins, E.M., Krupp, A.J., Perez de Arce, K., Ghosh, A.K., Fogel, A.I., Boucard, A., Sudhof, T.C., Stein, V., and Biederer, T. (2010). SynCAM 1 adhesion dynamically regulates synapse number and impacts plasticity and learning. Neuron *68*, 894-906.

Sato, S., Inoue, T., Terada, K., Matsuo, I., Aizawa, S., Tano, Y., Fujikado, T., and Furukawa, T. (2007). Dkk3-Cre BAC transgenic mouse line: a tool for highly efficient gene deletion in retinal progenitor cells. Genesis *45*, 502-507.

Sato, S., Omori, Y., Katoh, K., Kondo, M., Kanagawa, M., Miyata, K., Funabiki, K., Koyasu, T., Kajimura, N., Miyoshi, T.*, et al.* (2008). Pikachurin, a dystroglycan ligand, is essential for photoreceptor ribbon synapse formation. Nat Neurosci *11*, 923-931.

Schiller, P.H. (1992). The ON and OFF channels of the visual system. Trends Neurosci *15*, 86-92.

Schiller, P.H. (2010). Parallel information processing channels created in the retina. Proc Natl Acad Sci U S A *107*, 17087-17094.

Sharma, S., Ball, S.L., and Peachey, N.S. (2005). Pharmacological studies of the mouse cone electroretinogram. Vis Neurosci *22*, 631-636.

Shen, Y., Rampino, M.A., Carroll, R.C., and Nawy, S. (2012). G-protein-mediated inhibition of the Trp channel TRPM1 requires the Gbetagamma dimer. Proc Natl Acad Sci U S A *109*, 8752-8757.

Sherry, D.M., Wang, M.M., Bates, J., and Frishman, L.J. (2003). Expression of vesicular glutamate transporter 1 in the mouse retina reveals temporal ordering in development of rod vs. cone and ON vs. OFF circuits. J Comp Neurol *465*, 480-498.

Shirato, S., Maeda, H., Miura, G., and Frishman, L.J. (2008). Postreceptoral contributions to the light-adapted ERG of mice lacking b-waves. Exp Eye Res *86*, 914-928.

Stahl, J.S. (2004). Using eye movements to assess brain function in mice. Vision Res *44*, 3401-3410.

Stenzel, N., Fetzer, C.P., Heumann, R., and Erdmann, K.S. (2009). PDZ-domain-directed basolateral targeting of the peripheral membrane protein FRMPD2 in epithelial cells. J Cell Sci *122*, 3374-3384.

Sterling, P., and Matthews, G. (2005). Structure and function of ribbon synapses. Trends Neurosci *28*, 20-29.

Sudhof, T.C. (2008). Neuroligins and neurexins link synaptic function to cognitive disease. Nature *455*, 903-911.

Sugita, Y., Araki, F., Chaya, T., Kawano, K., Furukawa, T., and Miura, K. (2015). Role of the mouse retinal photoreceptor ribbon synapse in visual motion processing for optokinetic responses. PLoS One *10*, e0124132.

Sugita, Y., Miura, K., Araki, F., Furukawa, T., and Kawano, K. (2013). Contributions of retinal direction-selective ganglion cells to optokinetic responses in mice. Eur J Neurosci *38*, 2823-2831.

Sylwestrak, E.L., and Ghosh, A. (2012). Elfn1 regulates target-specific release probability at CA1-interneuron synapses. Science *338*, 536-540.

Tabata, H., Shimizu, N., Wada, Y., Miura, K., and Kawano, K. (2010). Initiation of the optokinetic response (OKR) in mice. J Vis *10*, 13 11-17.

tom Dieck, S., and Brandstatter, J.H. (2006). Ribbon synapses of the retina. Cell Tissue Res *326*, 339-346.

Tomioka, N.H., Yasuda, H., Miyamoto, H., Hatayama, M., Morimura, N., Matsumoto, Y., Suzuki, T., Odagawa, M., Odaka, Y.S., Iwayama, Y.*, et al.* (2014). Elfn1 recruits presynaptic

mGluR7 in trans and its loss results in seizures. Nat Commun *5*, 4501.

Ueda, Y., Iwakabe, H., Masu, M., Suzuki, M., and Nakanishi, S. (1997). The mGluR6 5' upstream transgene sequence directs a cell-specific and developmentally regulated expression in retinal rod and ON-type cone bipolar cells. J Neurosci *17*, 3014-3023.

Uemura, T., Lee, S.J., Yasumura, M., Takeuchi, T., Yoshida, T., Ra, M., Taguchi, R., Sakimura, K., and Mishina, M. (2010). Trans-synaptic interaction of GluRdelta2 and Neurexin through Cbln1 mediates synapse formation in the cerebellum. Cell *141*, 1068-1079.

Wan, G., Gomez-Casati, M.E., Gigliello, A.R., Liberman, M.C., and Corfas, G. (2014). Neurotrophin-3 regulates ribbon synapse density in the cochlea and induces synapse regeneration after acoustic trauma. Elife *3*.

Wassle, H. (2004). Parallel processing in the mammalian retina. Nat Rev Neurosci *5*, 747-757.

Wassle, H., Puller, C., Muller, F., and Haverkamp, S. (2009). Cone contacts, mosaics, and territories of bipolar cells in the mouse retina. J Neurosci *29*, 106-117.

Watanabe, S., Sanuki, R., Sugita, Y., Imai, W., Yamazaki, R., Kozuka, T., Ohsuga, M., and Furukawa, T. (2015). Prdm13 regulates subtype specification of retinal amacrine interneurons and modulates visual sensitivity. J Neurosci *35*, 8004-8020.

Werblin, F.S., and Dowling, J.E. (1969). Organization of the retina of the mudpuppy, Necturus maculosus. II. Intracellular recording. J Neurophysiol *32*, 339-355.

Xu, Y., Orlandi, C., Cao, Y., Yang, S., Choi, C.I., Pagadala, V., Birnbaumer, L., Martemyanov, K.A., and Vardi, N. (2016). The TRPM1 channel in ON-bipolar cells is gated by both the alpha and the betagamma subunits of the G-protein Go. Sci Rep *6*, 20940.

Zeitz, C., Jacobson, S.G., Hamel, C.P., Bujakowska, K., Neuille, M., Orhan, E., Zanlonghi, X., Lancelot, M.E., Michiels, C., Schwartz, S.B.*, et al.* (2013). Whole-exome sequencing identifies LRIT3 mutations as a cause of autosomal-recessive complete congenital stationary night blindness. Am J Hum Genet *92*, 67-75.

Figures and Legends

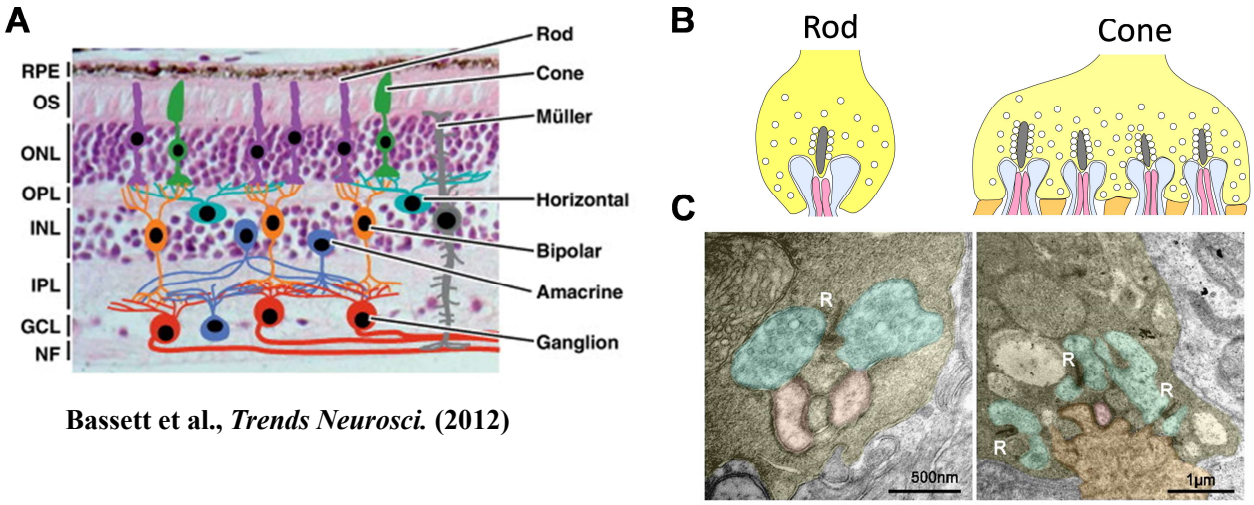

Bassett et al., *Trends Neurosci.* (2012)

Furukawa et al., *Cell Mol Life Sci.* (2019)

Figure G1. Structures of the retina and photoreceptor synapses.

(A) Schematic diagram of the vertebrate retina. Rod, rod photoreceptor cell; Cone, cone photoreceptor cell; Bipolar, bipolar cell; Horizontal, horizontal cell; Amacrine, amacrine cell; Ganglion, ganglion cell; Müller, müller glia cell.

(B) Schematic of rod (left panel) and cone (right panel) photoreceptor synaptic structures. Photoreceptor synapses contain a synaptic ribbon (gray), which tethers synaptic vesicles (white circles) to the surface. ON-bipolar cell dendritic terminals (pink) and horizontal cell processes (blue) invaginate the photoreceptor axon terminals (yellow). OFF-bipolar cell dendrites (orange) make a flat, non-invaginating connection with cone photoreceptor axon terminals.

(C) Electron micrographs of rod (left panel) and cone (right panel) photoreceptor axon terminals in WT mouse retina at 1M. Photoreceptor axonal terminals are colored yellow, horizontal cell processes are colored blue, and bipolar cell dendritic terminals are colored pink. R indicates the synaptic ribbon.

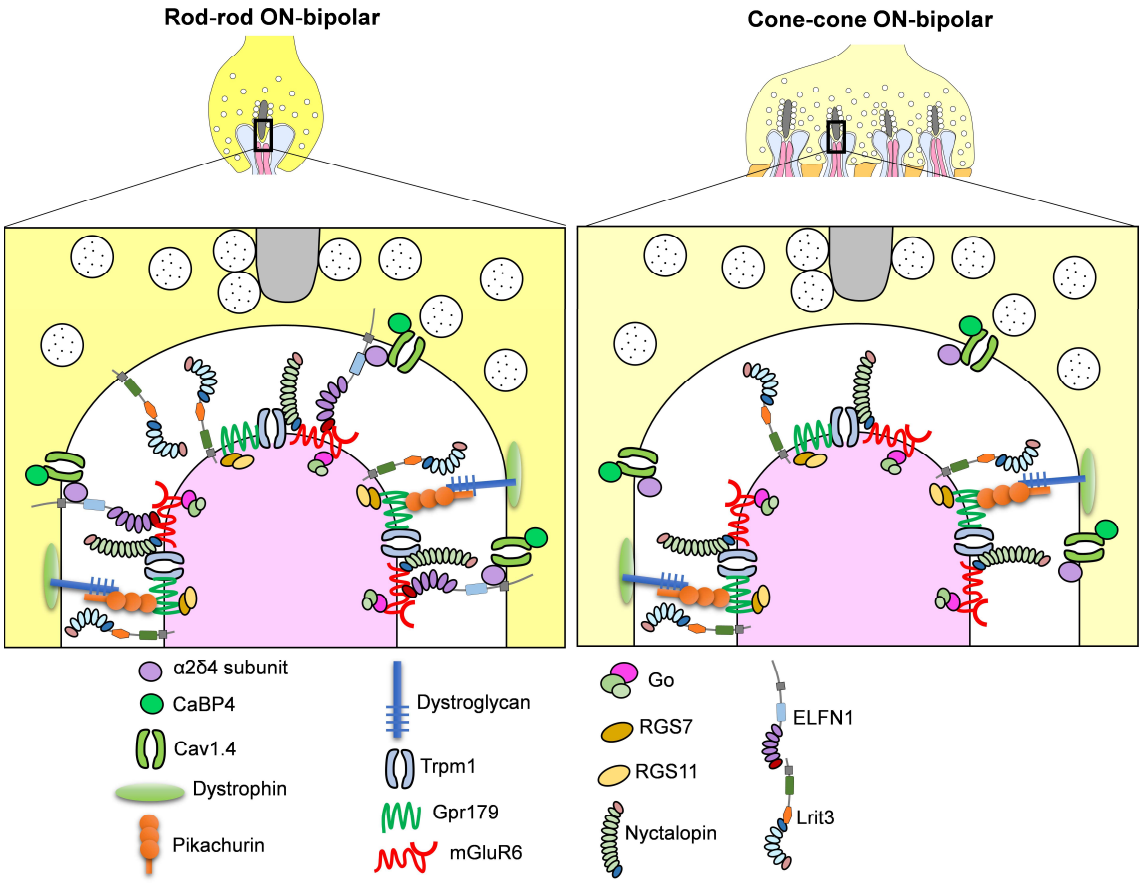

Furukawa et al., *Cell Mol Life Sci.* (2019), modified

Figure G2. Proposed model of the rod and cone photoreceptor synapse formation.

The molecules involved in synapse formation between photoreceptor cells and ON-bipolar cells. The left panel indicates rod photoreceptor synapses and the right panel indicates cone photoreceptor synapses.

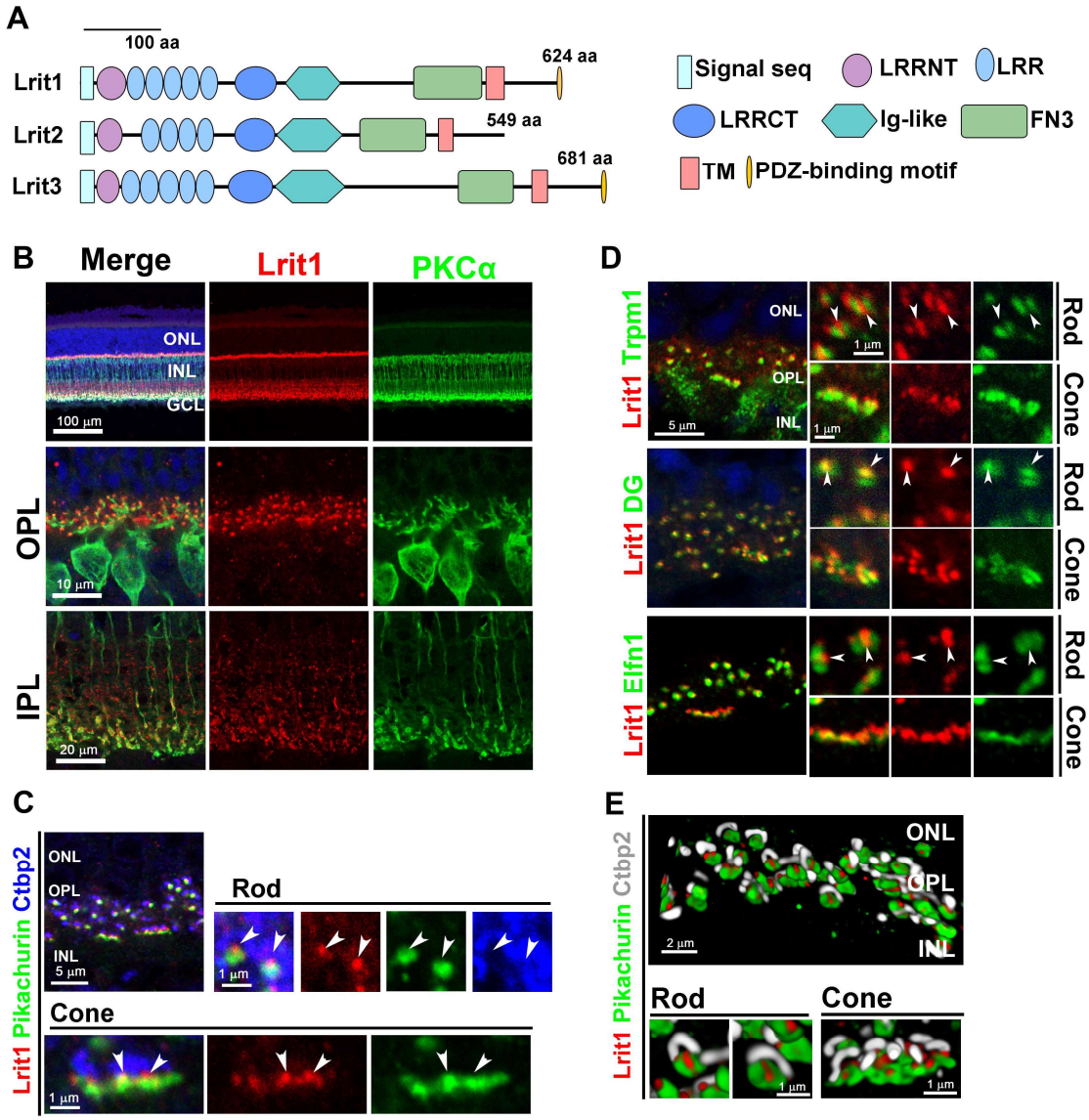

Figure 1. Lrit1 localizes at photoreceptor and bipolar cell-synaptic terminals in the OPL and IPL, respectively.

(A) Domain structures of Lrit family proteins. The proteins contain extracellular N-terminal Leucine-rich repeat (LRRNT), Leucine-rich repeat (LRR), C-terminal LRR (LRRCT), Fibronectin type 3 (FN3), and Immunoglobulin (Ig)-like domains, followed by a transmembrane domain and intracellular C-terminals. A PDZ-binding motif is present in the C-terminal intracellular domains of Lrit1 and Lrit3, but not in Lrit2.

(B) Immunostaining of WT retinal section at 1M using anti-Lrit1 (red) and anti-PKCα (rod ON-bipolar cell marker, green) antibodies. Lrit1 partially co-localized with PKCα in the OPL, and localized to ON- and OFF-bipolar cell axon terminals in the IPL.

(C) Lrit1 localizes at the subregion of photoreceptor synaptic terminals. The 1M WT retinal sections were immunostained with anti-Lrit1 (red, arrowheads), anti-Pikachurin (green) and anti-Ctbp2 (blue) antibodies. Lrit1 localizes to the subregion sandwiched between Ctbp2-positive ribbons and synaptic clefts immunostained with Pikachurin.

(D) Lrit1 localizes at a unique subregion of photoreceptor synaptic terminals. The WT retinal sections were immunostained with anti-Lrit1 (red), anti-Trpm1 (green, upper panels), anti-Dystroglycan (DG, green, middle panels), and anti-Elfn1 (green, lower panels) antibodies. The Lrit1 signals partially overlapped, but not completely, with synaptic markers Elfn1, Dystroglycan, and Trpm1.

(E) 3D-SIM images of photoreceptor synapses immunostained using anti-Lrit1 (red), anti-Pikachurin (green), and anti-Ctbp2 (white) antibodies. Lrit1 localizes to the narrow membrane region between two bipolar cell dendritic tips. ONL, outer nuclear layer; INL, inner nuclear layer; GCL, ganglion cell layer; OPL, outer plexiform layer; IPL, inner plexiform layer. See also Figure S1.

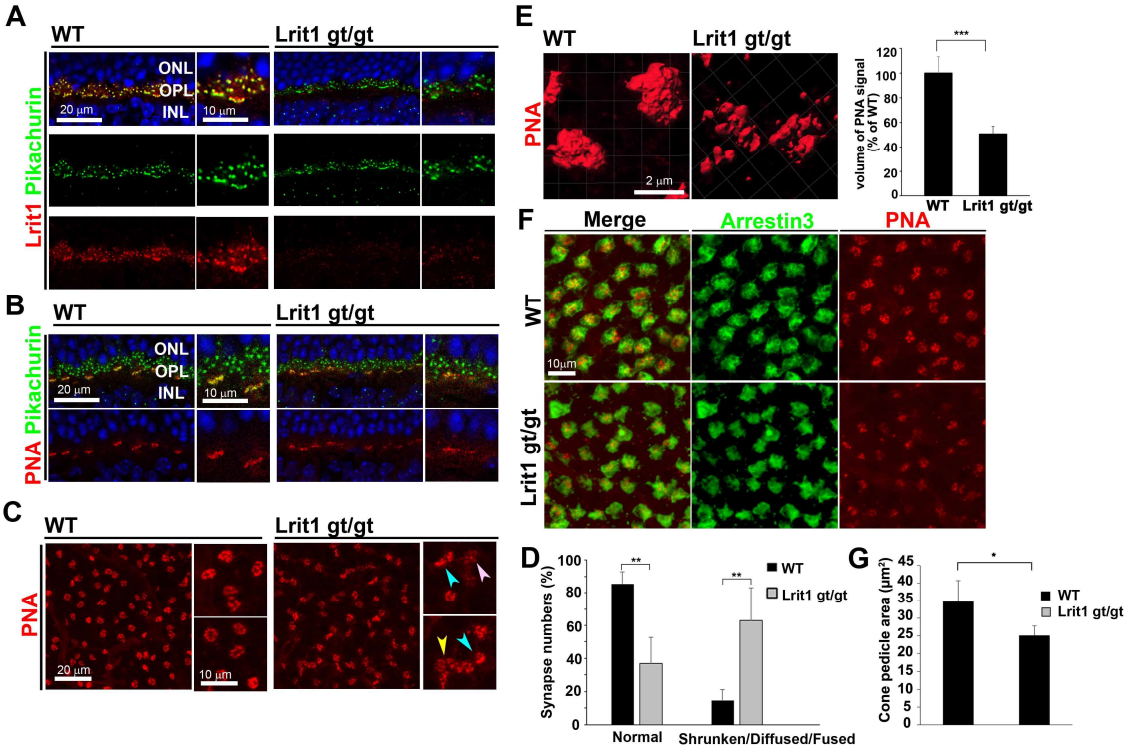

Figure 2. The loss of *Lrit1* causes morphological defects in cone photoreceptor synaptic terminals.

(A) Retinal sections from WT and *Lrit1*$^{gt/gt}$ mice at 1M were immunostained with anti-Lrit1 (red) and anti-Pikachurin (green) antibodies, and DAPI (blue). The Lrit1 signals in the OPL disappeared in the *Lrit1*$^{gt/gt}$ mice. The localization of Pikachurin was unaltered in the *Lrit1*$^{gt/gt}$ retina.

(B) Staining of WT and *Lrit1*$^{gt/gt}$ retinas with the anti-Pikachurin antibody (green) and PNA-rhodamine (red).

(C) Retinal flat-mount immunostaining of WT and *Lrit1*$^{gt/gt}$ mice with PNA-rhodamine (red). The morphological abnormalities of the PNA signals, such as diffused (pink arrowhead), shrunken (blue arrowhead), and fused (yellow arrowhead), were observed in the *Lrit1*$^{gt/gt}$ retina.

(D) Quantification of normal and abnormal morphological cone photoreceptor synaptic

terminals in WT control (n=3) and *Lrit1*$^{gt/gt}$ (n=3) mice. The numbers of abnormal morphological cone synaptic terminals increased in the *Lrit1*$^{gt/gt}$ retina.

ONL, outer nuclear layer; OPL, outer plexiform layer; INL, inner nuclear layer.

(E) Quantification of the volume of cone synapse terminals stained with PNA in WT control (n=3) and *Lrit1*$^{gt/gt}$ (n=3) retinas by 3D-SIM analysis. The volume of cone synaptic terminals in the OPL was reduced to 50.7% in the *Lrit1*$^{gt/gt}$ retina.

(F, G) Flat-mount immunostaining of WT (n=3) and *Lrit1*$^{gt/gt}$ (n=4) retinas using rhodamine-labeled PNA (red) and an anti-Arrestin3 (green) antibody. Cone pedicle size was quantified using MetaMorph software (WT; n=3, *Lrit1*$^{gt/gt}$; n=4, 45 pedicles from each animal). Cone pedicle size in the *Lrit1*$^{gt/gt}$ retina was significantly smaller than that of the WT retina. Error bars show the SD. *P<0.05, **P<0.03, ***P<0.01. See also Figure S1-S5.

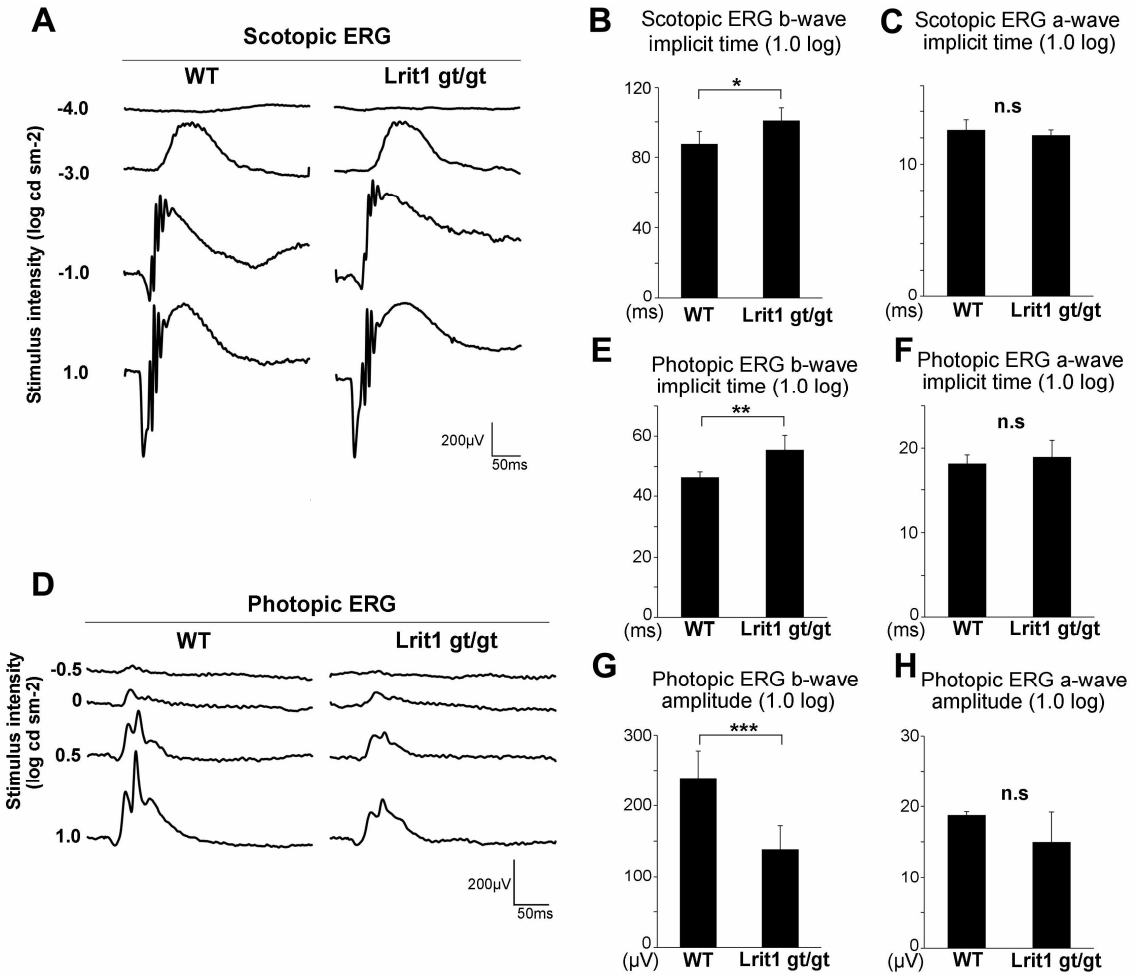

Figure 3. Electrophysiological analysis of WT control and *Lrit1*$^{gt/gt}$ mice.

(A-H) ERGs were recorded from WT control (n=4) and *Lrit1*$^{gt/gt}$ mice (n=4) at 1M. Representative dark-adapted (scotopic) ERGs in WT and *Lrit1*$^{gt/gt}$ mice elicited by four different stimulus intensities (-4.0, -3.0, -1.0 and 1.0 log cd sm^{-2}) are presented **(A)**. The implicit time of the scotopic ERG b-wave as a function of the stimulus intensity (1.0 log cd sm^{-2}) was prolonged in *Lrit1*$^{gt/gt}$ mice **(B)**, but that of the scotopic ERG a-wave was unaltered between WT and *Lrit1*$^{gt/gt}$ mice **(C)**. Representative light-adapted (photopic) ERGs in WT and *Lrit1*$^{gt/gt}$ mice elicited by four different stimulus intensities (-0.5, 0, 0.5, and 1.0 log cd sm^{-2}) are presented **(D)**. The implicit time of the photopic ERG b-wave as a function of the stimulus intensity (-0.5, 0, 0.5 and 1.0 log cd sm^{-2}) was prolonged in

Lrit1$^{gt/gt}$ mice **(E)**, but that of the photopic ERG a-wave was unaltered **(F)**. The amplitude of the photopic ERG b-wave as a function of the stimulus intensity (0.5 and 1.0 log cd sm^{-2}) was decreased in *Lrit1*$^{gt/gt}$ mice **(G)**, but that of a-wave was unaltered **(H)**. Error bars show the SD. **P*<0.05, ***P*<0.03, ****P*<0.01. See also Figure S1-S4 and S6.

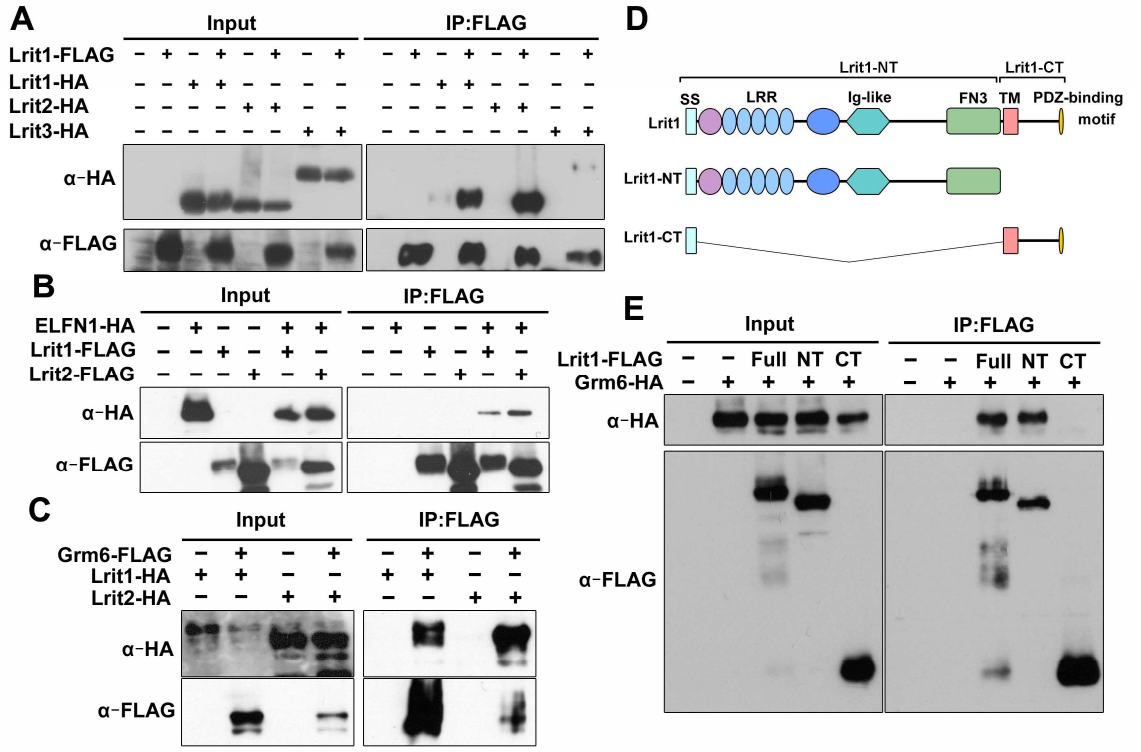

Figure 4. Lrit1 and Lrit2 interact with Grm6.

(A) Immunoprecipitation analysis of each Lrit family member (Lrit1, Lrit2, and Lrit3) and Lrit1. Plasmids expressing each HA-tagged Lrit family member were transfected into HEK293 cells with the plasmid expressing FLAG-tagged Lrit1. Strong interactions of Lrit1 with itself and Lrit2, and a very weak interaction of Lrit1 with Lrit3 were observed. **(B)** Immunoprecipitation analysis of Lrit1 or Lrit2 with Elfn1. A plasmid expressing Lrit1-FLAG or Lrit2-FLAG was transfected into HEK293 cells along with a plasmid expressing Elfn1-HA. Lrit1-FLAG or Lrit2-FLAG was immunoprecipitated with the anti-FLAG antibody. Elfn1-HA was co-immunoprecipitated with Lrit1-FLAG or Lrit2-FLAG. **(C)** Co-immunoprecipitation of Lrit1 or Lrit2 with Grm6. A plasmid expressing FLAG-tagged Grm6 was transfected into HEK293 cells with the plasmid expressing HA-tagged Lrit1 or HA-tagged Lrit2. Grm6-FLAG was immunoprecipitated with the anti-FLAG antibody. HA-tagged Lrit1 and HA-tagged Lrit2 co-immunoprecipitated with Grm6-

FLAG.

(D) Schematic diagrams of Lrit1 truncated mutants. FLAG-tagged N- or C-terminal portion of Lrit1 (Lrit1-NT, -CT) were expressed with HA-tagged Grm6 in HEK293T cells.

(E) Immunoprecipitation analysis of Lrit1 truncated mutants and Grm6. Lrit1-NT and Lrit1-CT were immunoprecipitated with the anti-FLAG antibody. HA-tagged Grm6 co-immunoprecipitated with Lrit1-NT but not with Lrit1-CT.

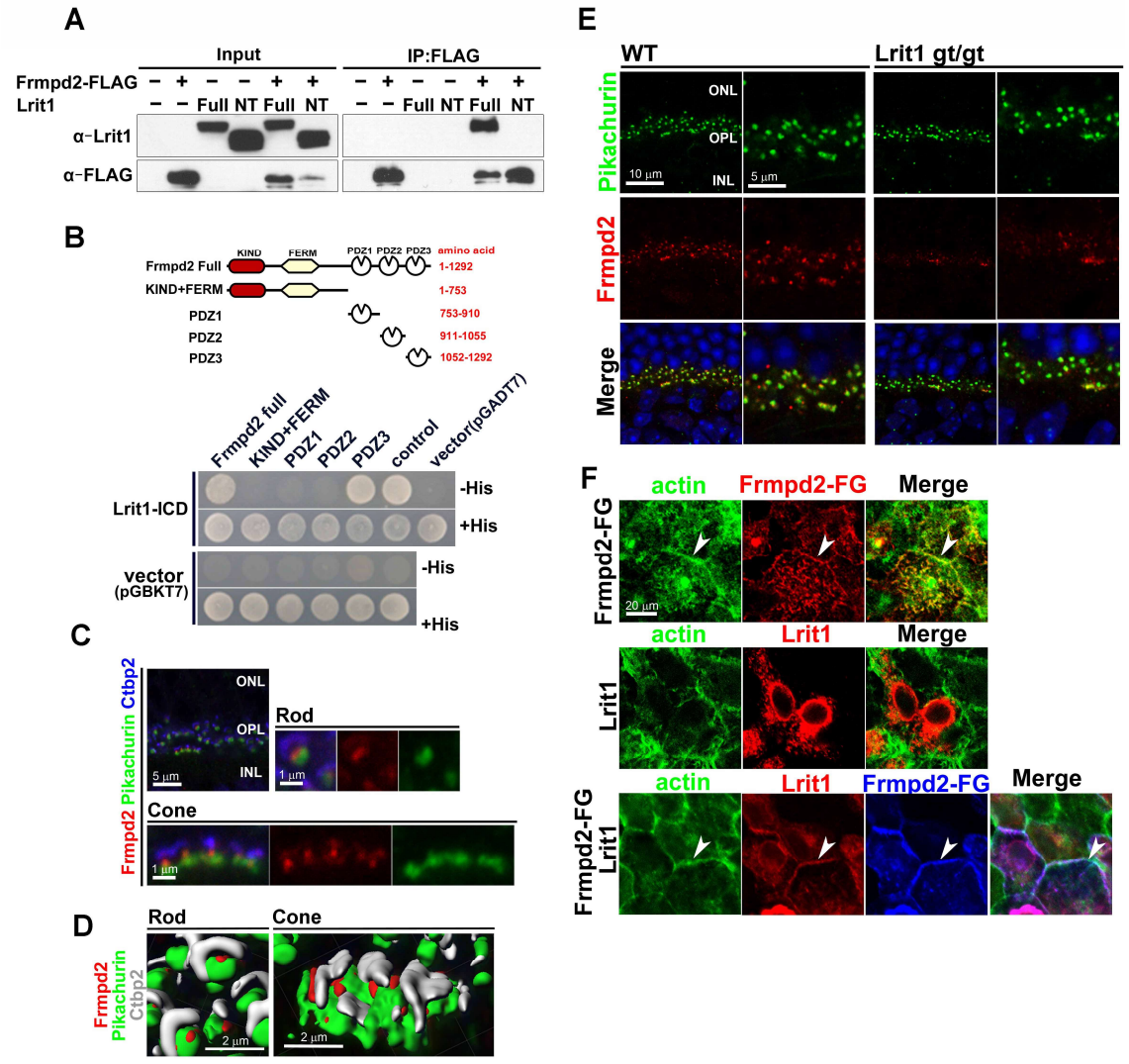

Figure 5. Lrit1 interacts with Frmpd2.

(A) Immunoprecipitation analysis of Lrit1 and Frmpd2. A plasmid expressing Frmpd2-FLAG was transfected into HEK293 cells along with a plasmid expressing the full length Lrit1 or Lrit1-NT. Frmpd2-FLAG was immunoprecipitated with the anti-FLAG antibody. Full-length Lrit1 but not Lrit1-NT was co-immunoprecipitated with Frmpd2-FLAG.

(B) The third PDZ domain of Frmpd2 interacts with the Lrit1 C-terminal domain. Schematic diagrams of Frmpd2-deletion mutants were shown. The intracellular domain of Lrit1 was used as the bait in a yeast two-hybrid assay. Five Frmpd2 constructs were used as preys: full length (Frmpd2-Full), KIND and FERM domain (KIND+FERM),

PDZ1 domain (PDZ1), PDZ2 domain (PDZ2), and PDZ3 domain (PDZ3). Only the Frmpd2-Full and PDZ3 interacted with the Lrit1 intracellular domain.

(C) Immunostaining of 4 week WT retina with anti-Frmpd2 (red), anti-Ctbp2 (blue) and anti-Pikachurin (green) antibodies. Puncta of Frmpd2 localized at the synaptic subregion between Ctbp2-positive ribbons and Pikachurin-positive photoreceptor synaptic clefts in the OPL.

(D) 3D-SIM images of photoreceptor synapses immunostained with anti-Frmpd2 (red), anti-Pikachurin (green), and anti-Ctbp2 (white) antibodies. Similarly to Lrit1, Frmpd2 localizes to the narrow membrane region just outside of the synaptic ribbon, which is confined between bipolar cell dendritic tips.

(E) Immunostaining of the 1M WT control and *Lrit1*$^{gt/gt}$ retinas with anti-Frmpd2 (red) and anti-Pikachurin (green) antibodies. The Frmpd2 signals in the OPL were markedly reduced in the *Lrit1*$^{gt/gt}$ mice.

(F) Co-localization of Lrit1 and actin cytoskeletons in a Frmpd2 dependent manner. The plasmid expressing Lrit1 was transfected into HEK293 cells with or without the plasmid expressing Frmpd2-FLAG. Cells were immunostained with anti-FLAG (blue/red) and anti-Lrit1 (red) antibodies with Phalloidin (green). Lrit1 co-localized with Frmpd2 at the submembrane region in a Frmpd2-dependent manner. ONL, outer nuclear layer; OPL, outer plexiform layer; INL, inner nuclear layer. See also Figure S6.

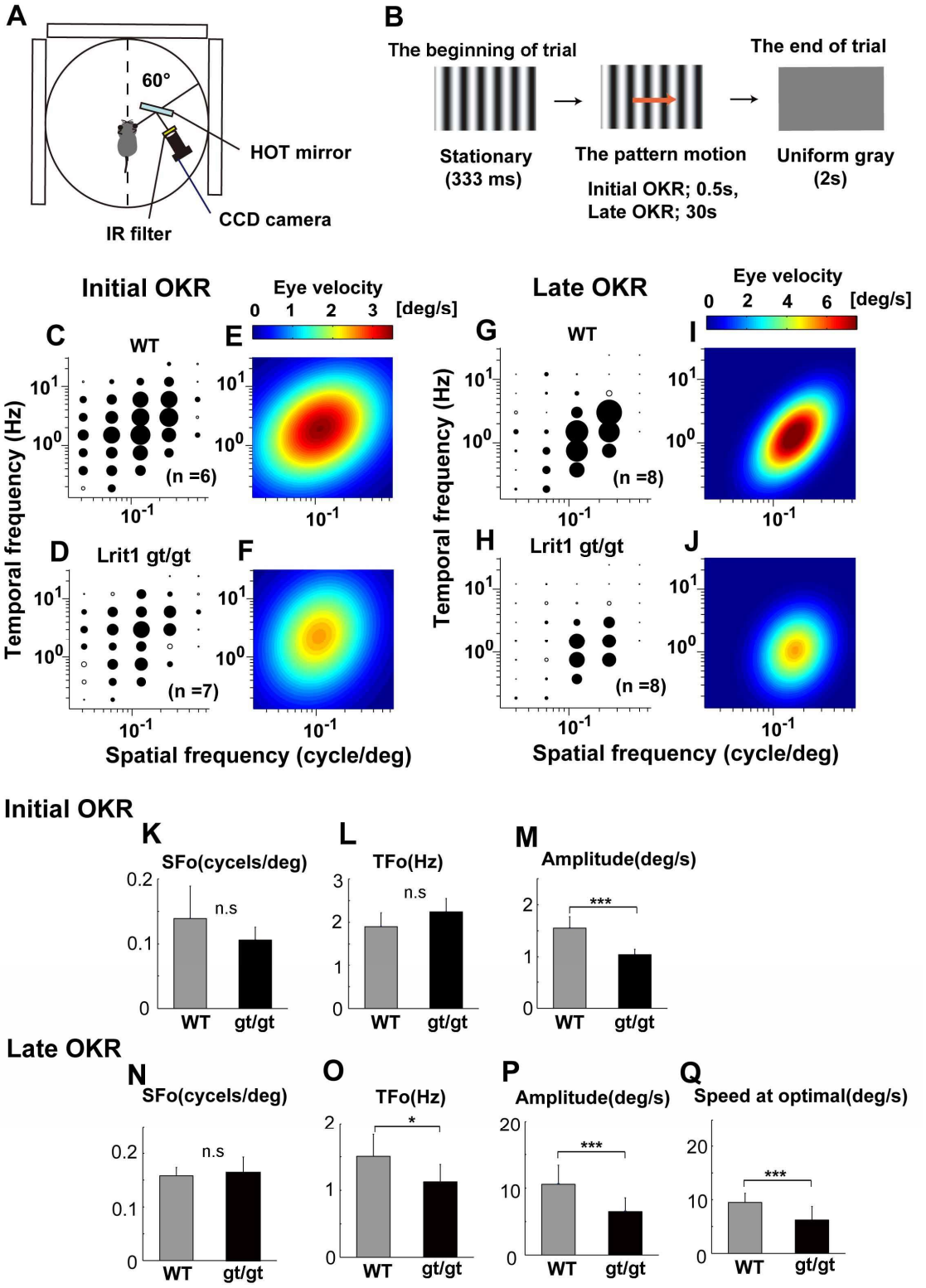

Figure 6. *Lrit1*$^{gt/gt}$ mice exhibit impaired visual sensitivities in OKRs.

(A, B) Schematic representation of OKR testing apparatus and procedures. A mouse was

placed on a platform, and moving gratings were displayed on computer monitors surrounding the mouse **(A)**. A visual stimulus was presented on three LCD monitors set around the mouse (19-inch LCD, refresh rate: 75Hz, size: 270°×65.7°). At the beginning of each trial, a stationary visual pattern was presented, and then moved counterclockwise or clockwise at a constant speed for 100-200 ms (initial OKR) or 1-30 s (late OKR; OKN). After a defined period, the pattern was removed **(B)**.

(C-F) Amplitudes of the initial OKRs in WT control (n=6) and *Lrit1*$^{gt/gt}$ (n=7) mice at 2-4 months old were measured. Amplitudes of the initial OKR are represented by the diameter of circles plotted in the coordinate system of spatial and temporal frequencies (SF and TF, respectively). Filled symbols represent statistically significant responses (t-test, $p < 0.05$) **(C, D).** Heat map plots of the best-fit Gaussian functions for the initial OKRs in WT **(E)** and *Lrit1*$^{gt/gt}$ **(F)** mice are displayed.

(G-J) Amplitudes of the late OKRs in WT (n=8) and *Lrit1*$^{gt/gt}$ (n=8) mice at 2-4 months old were measured. Filled symbols represent statistically significant responses (t-test, $p < 0.05$) **(G, H).** Heat map plots of the best-fit Gaussian functions for the late OKRs in WT **(I)** and *Lrit1*$^{gt/gt}$ **(J)** mice are shown.

(K-M) Comparisons of the properties of the initial OKRs in WT (n=6) and *Lrit1*$^{gt/gt}$ (n=7) mice. The optimal spatial frequency **(K)**, temporal frequency **(L)** and amplitude **(M)** in initial OKRs in WT and *Lrit1*$^{gt/gt}$ mice are shown.

(**N-Q) C**omparisons of the properties of the late OKRs WT (n=8) and *Lrit1*$^{gt/gt}$ (n=8) mice. The optimal spatial frequency **(N)**, temporal frequency **(O)**, amplitude **(P)**, and speeds at the optimal stimulus **(Q)** in late OKRs in WT and *Lrit1*$^{gt/gt}$ mice are shown. Error bars show the SD. **P*<0.05, ****P*<0.01. See also Figure S7.

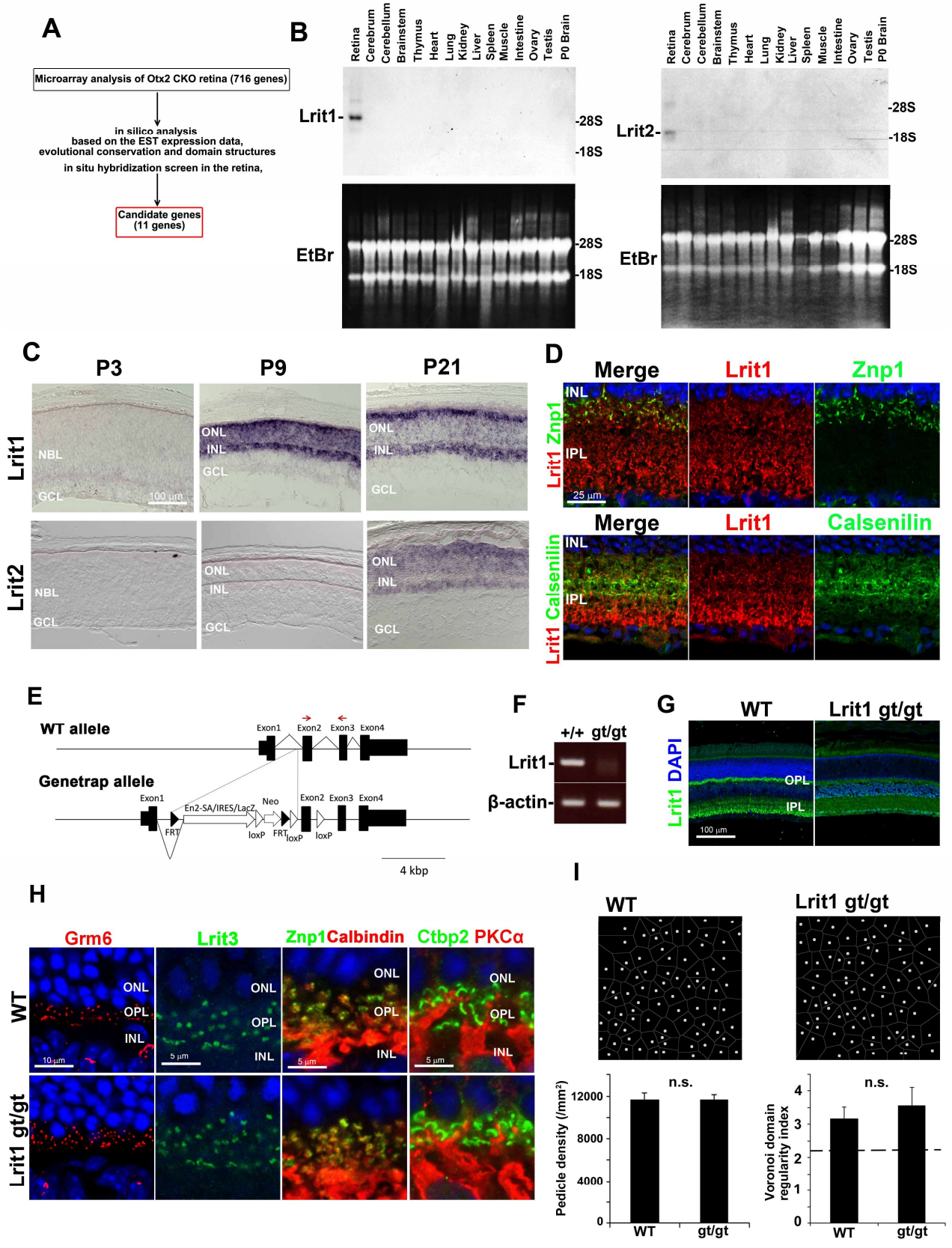

Figure S1. Expression of *Lrit1* and *Lrit2* in the mouse retina and generation of the

***Lrit1*$^{gt/gt}$ mice, Related to Figure 1-3.**

(A) Strategy of the screen for candidate genes involved in photoreceptor synapse formation and/or maintenance. To identify genes regulating retinal photoreceptor synapse formation, a microarray analysis of *Otx2* conditional knockout (CKO) mouse retina was carried out. Genes enriched in photoreceptor cells decrease in the *Otx2* CKO retinas. Expression of 716 genes decreased in *Otx2* CKO retina. From the downregulated genes in the *Otx2* CKO retina, *in silico* analysis was performed based on the EST expression data, evolutional conservation, and domain structures. After *in situ* hybridization screen of candidate genes in the retina, I selected 11 candidate genes for regulation of retinal synapse formation.

(B) Northern blot analysis of *Lrit1* and *Lrit2* in 1M mouse tissues. The distribution of *Lrit1* and *Lrit2* mRNA among mouse tissues (upper panel) and ethidium bromide (EtBr) staining of the RNA (lower panel). 18S and 28S rRNAs are indicated. *Lrit1* and *Lrit2* were specifically expressed in the retina.

(C) *In situ* hybridization analysis of *Lrit1* and *Lrit2* in developing (P3, P9) and mature (P21) mouse retinas. *Lrit1* and *Lrit2* were expressed photoreceptor and bipolar cells in the adult retina. *Lrit1* signal was below detection level at P3. *Lrit1* expression was observed at high levels in the ONL and INL at P9 and P21. *Lrit2* was expressed in the ONL and INL at P21. *Lrit2* signal was below detection level at P3 and P9.

(D) Immunostaining of 1M WT retina using anti-Lrit1 (red), anti-Znp1 (a type 2 cone OFF-bipolar synapse marker, green, upper panel), and anti-Calsenilin (a type 4 cone OFF-bipolar synapse marker, green, lower panel) antibodies. Lrit1 partially co-localized with Znp1 and Calsenilin in the IPL.

(E) Schematic representation of the *Lrit1* WT allele and genetrap allele. The cassette containing a genetrap splice acceptor-*LacZ* was inserted between exon 1 and exon 2 of *Lrit1*. The genetrap splice acceptor was designed to capture the nascent RNA results in truncation of the transcript downstream of the cassette. Red arrows indicate primers to detect *Lrit1* in WT mice.

(F) RT-PCR analysis of *Lrit1* transcription in WT control and *Lrit1*$^{gt/gt}$ retinas. The primers were designed within exon 2 and exon 3 of *Lrit1*. No *Lrit1* transcript was detected in the *Lrit1*$^{gt/gt}$ retina.

(G) Immunostaining of WT and *Lrit1*$^{gt/gt}$ retinas with an anti-Lrit1 antibody (green). No significant Lrit1 signal was observed in the OPL and IPL of the *Lrit1*$^{gt/gt}$ retina.

(H) Immunofluorescent analysis of WT and *Lrit1*$^{gt/gt}$ retinas using anti-Grm6 (an ON-bipolar cell synapse marker, red in left panels), anti-Lrit3 (an ON-bipolar cell synapse marker, green in second left panels), anti-Znp1 (a type 2 cone OFF-bipolar synapse

marker, green in second right panels), anti-Calbindin (a horizontal cell synapse marker, red in second right panels), anti-Ctbp2 (a photoreceptor synapse marker, green in right panels), and anti-PKCα (a rod bipolar cell marker, red in right panels) antibodies. Nuclei were stained with DAPI (blue). No obvious change was observed between WT and *Lrit1*$^{gt/gt}$ retinas.

(I) Density of cone pedicles is unchanged between WT and *Lrit1*$^{gt/gt}$ retinas. The Voronoi domain regularity index is not significantly different between WT (n=3) and *Lrit1*$^{gt/gt}$ (n=3) retinas. The broken line indicates an estimated index value for supposed random cell distribution. Error bars show the SD. NBL, neuroblastic layer; ONL, outer nuclear layer; OPL, outer plexiform layer; INL, inner nuclear layer; IPL, inner plexiform layer; GCL, ganglion cell layer.

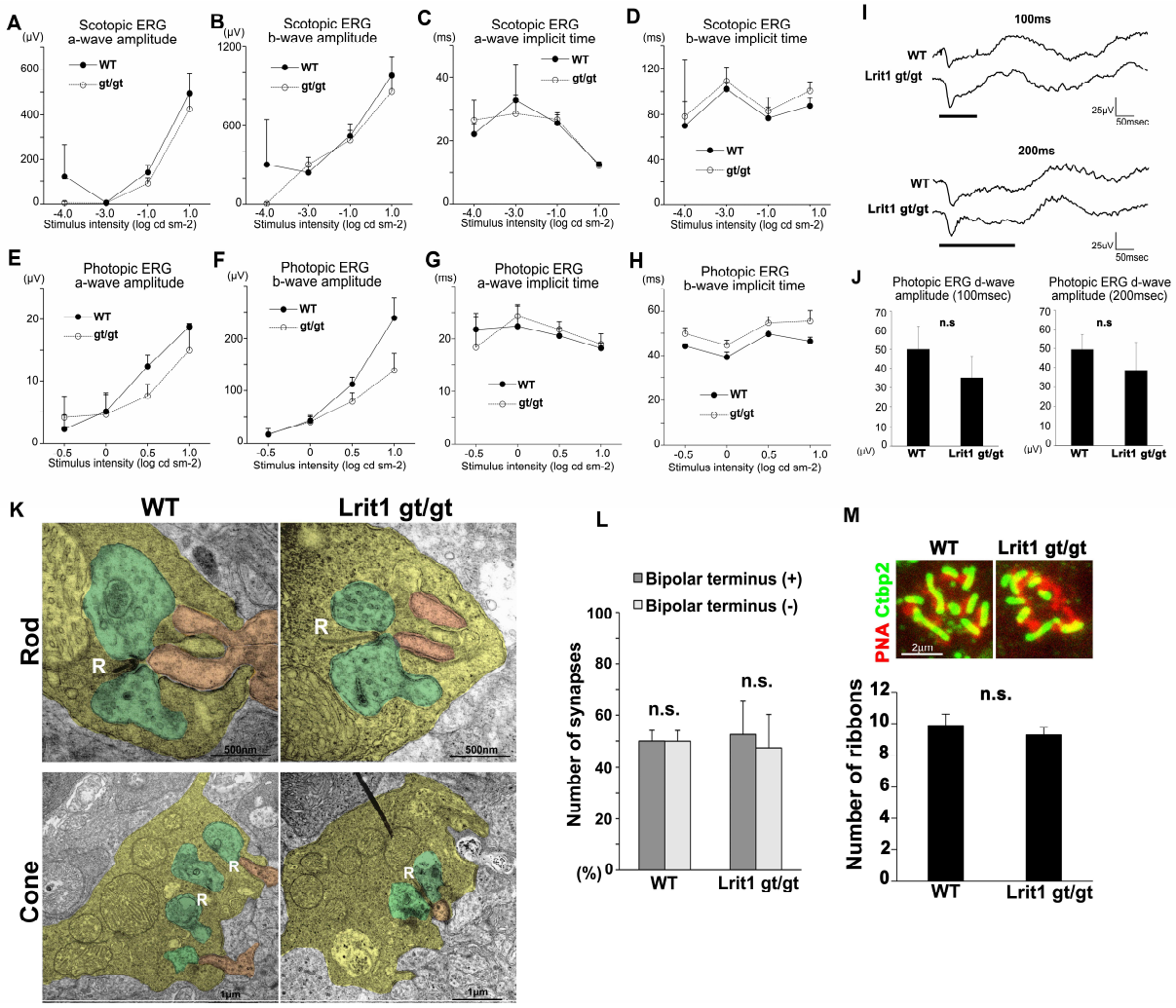

Figure S2. ERG and ultrastructural analysis of WT control and *Lrit1*$^{gt/gt}$ retinas, Related to Figure 2 and 3.

(A-H) Scotopic and photopic ERGs were recorded from WT control and *Lrit1*$^{gt/gt}$ mice at 1M. Representative scotopic **(A-D)** and photopic **(E-H)** ERGs elicited by four different stimulus intensities in WT (n=4) and *Lrit1*$^{gt/gt}$ (n=4) mice.

(I, J) The photopic ERGs in APB-injected WT and *Lrit1*$^{gt/gt}$ mice elicited by 100 or 200 msec stimulus duration. The stimulus luminance was constant at +0.5 log cd/m^2. No significant change was observed between WT (n=4) and *Lrit1*$^{gt/gt}$ (n=5) mice in ERG d-wave amplitudes.

(K) Electron microscopic analysis of photoreceptor ribbon synapses in the OPL of the *Lrit1*$^{gt/gt}$ retina. Normal invaginations of bipolar dendritic tips and horizontal processes were observed both of rod (upper panels) and cone (lower panels) photoreceptor synaptic terminals in the *Lrit1*$^{gt/gt}$ retina. Photoreceptor axonal terminals are colored in yellow, horizontal cell processes in green, and bipolar cell dendrites in pink. The black line in the

bottom right panel is likely heavy metal dust. R, synaptic ribbon.
(L) The percentages of rod photoreceptor axon terminals with or without bipolar dendritic tips in WT (n=3) and *Lrit1*$^{gt/gt}$ (n=3) retinas were quantified. **(M)** Quantification of the synaptic ribbon number in cone photoreceptor terminals in WT (n=3) and *Lrit1*$^{gt/gt}$ (n=3) retinas. Synaptic ribbons and cone synaptic terminals were stained with anti-Ctbp2 (green) and rhodamine-labeled PNA (red), respectively. The 3D images were reconstructed from z-stack images obtained by confocal microscopy. The numbers of cone synaptic ribbons were counted using 3D image. Error bars show the SD.

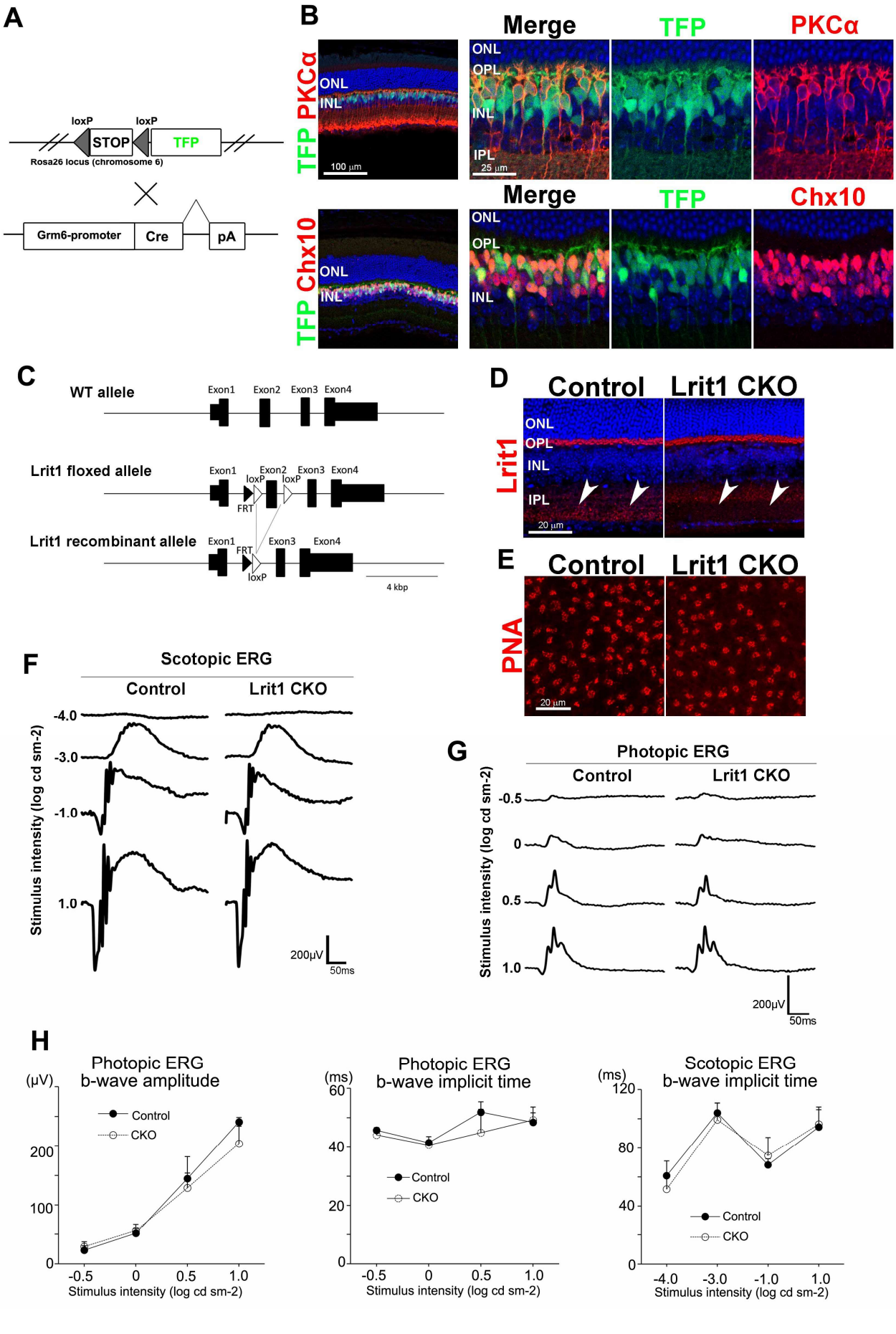
A
loxP
loxP
STOP
TFP
Rosa26 locus (chromosome 6)
Grm6-promoter
Cre
pA
B
Merge
TFP
PKCα
TFP PKCα
ONL
INL
100 μm
ONL
OPL
INL
IPL
25 μm
Merge
TFP
Chx10
TFP Chx10
ONL
INL
ONL
OPL
INL
C
WT allele
Exon1
Exon2
Exon3
Exon4
Lrit1 floxed allele
loxP
loxP
FRT
Lrit1 recombinant allele
FRT
loxP
4 kbp
D
Control
Lrit1 CKO
Lrit1
ONL
OPL
INL
IPL
20 μm
E
Control
Lrit1 CKO
PNA
20 μm
F
Scotopic ERG
Control
Lrit1 CKO
Stimulus intensity (log cd sm-2)
-4.0
-3.0
-1.0
1.0
200μV
50ms
G
Photopic ERG
Control
Lrit1 CKO
Stimulus intensity (log cd sm-2)
-0.5
0
0.5
1.0
200μV
50ms
H
Photopic ERG
b-wave amplitude
(μV)
Control
CKO
Stimulus intensity (log cd sm-2)
Photopic ERG
b-wave implicit time
(ms)
Control
CKO
Stimulus intensity (log cd sm-2)
Scotopic ERG
b-wave implicit time
(ms)
Control
CKO
Stimulus intensity (log cd sm-2)

Figure S3. Photoreceptor synapse formation and ERGs were not affected in ON-bipolar-specific *Lrit1* CKO mice, Related to Figure 2 and 3.

(A) A schematic diagram of *Grm6-Cre* and *ROSA26-TFP* alleles. *Grm6-Cre*; *ROSA26-TFP* mice were generated by crossing *Grm6-Cre* and *ROSA26-TFP* lines.

(B) Immunofluorescent staining of the *Grm6-Cre*; *ROSA26-TFP* mouse retina with anti-PKCα (a rod ON-bipolar cell marker, red, upper panels) and anti-Chx10 (a pan-bipolar cell marker, red, lower panels) antibodies. TFP signals (green) overlapped with PKCα and Chx10 signals. TFP was specifically expressed in ON-bipolar cells.

(C) A schematic diagram of the *Lrit1 floxed* and recombinant allele. $Lrit1^{fl/fl}$ mice were generated by crossing $Lrit1^{gt/gt}$ mice with *CAG-FLPe37* transgenic mice. *Lrit1* CKO mice were generated by crossing $Lrit1^{fl/fl}$ mice with *Grm6-Cre* transgenic mice. Removal of the floxed region by Cre mediated recombination is predicted to result in a premature stop codon and complete loss of the *Lrit1* function.

(D) Immunostaining of *Grm6-Cre* control and *Lrit1* CKO retinas with the anti-Lrit1 antibody (red). The Lrit1 signals in the ON-bipolar cell axon terminals (arrowheads) disappeared in the *Lrit1* CKO retina.

(E) Flat-mount immunostaining of control and *Lrit1* CKO retinas with rhodamine-conjugated PNA (red). No significant difference was observed between control and *Lrit1* CKO retinas.

(F-H) Scotopic and photopic ERGs recorded from control (n=3) and *Lrit1* CKO (n=3) mice at 1M. Representative scotopic **(F)** and photopic **(G)** ERGs elicited by four different stimulus intensities in control and *Lrit1* CKO mice. In scotopic and photopic ERGs, no significant change in the amplitude and implicit times between control and *Lrit1* CKO mice was observed **(H)**. These results suggest that Lrit1, which is expressed in photoreceptor cells, is essential for the photoreceptor synapse formation and responsible for the aberrant ERG phenotype. Error bars show the SD. ONL, outer nuclear layer; OPL, outer plexiform layer; INL, inner nuclear layer; IPL, inner plexiform layer.

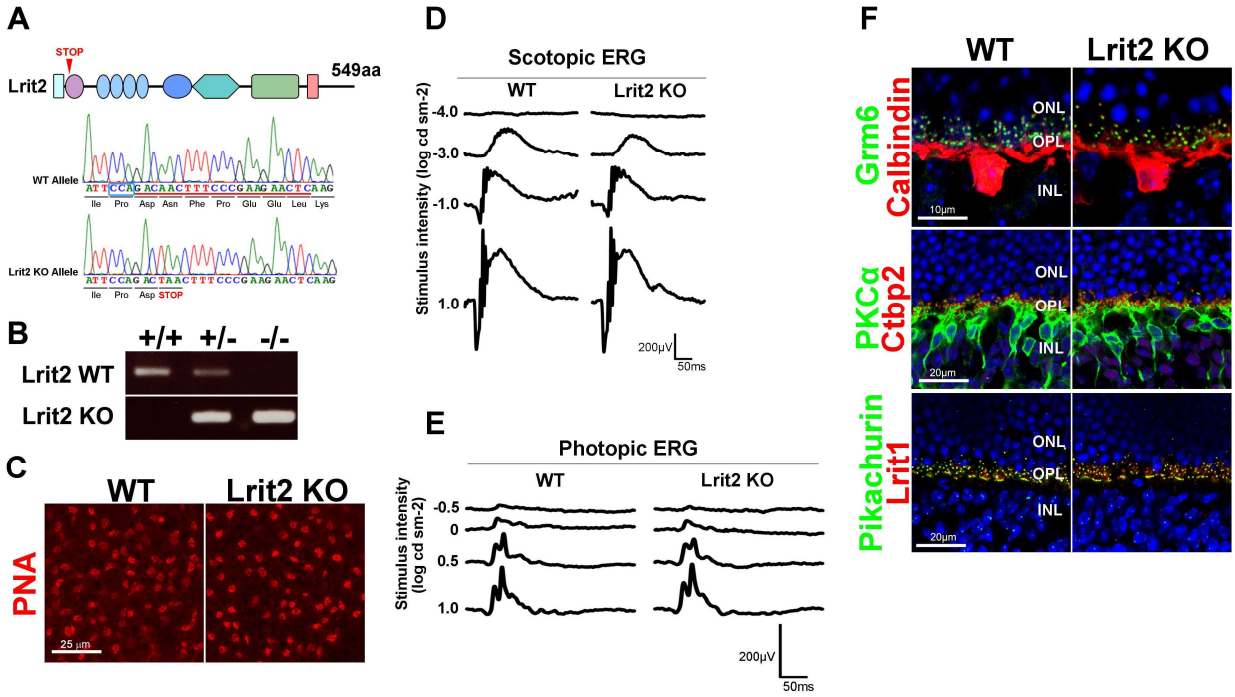

Figure S4. ERGs and photoreceptor synapse formation in the *Lrit2*$^{-/-}$ mouse retina, Related to Figure 2 and 3.

(A) Schematic Diagram (upper panel) and sequence around the mutation (lower panel) of *Lrit2*$^{-/-}$ mice. *Lrit2*$^{-/-}$ mouse was generated by CRISPR/Cas9-mediated gene editing. 1-bp insertion in *Lrit2* exon 2 results in a frame shift and a premature stop codon after the 51st amino acid residue of the Lrit2 N-terminal domain. The gRNA region was underlined in red. Blue box represents a PAM sequence.

(B) PCR products amplified from genomic DNA of the WT control and *Lrit2*$^{-/-}$ mice. Genotyping primers to amplify the WT or *Lrit2*$^{-/-}$ allele were designed to match the mutation site in the exon 2 of the *Lrit2* gene.

(C) Retinal flat-mount fluorescent staining of WT and *Lrit2*$^{-/-}$ mice with PNA-rhodamine (red). No significant change was observed in the *Lrit2*$^{-/-}$ retina.

(D, E) ERGs recorded from WT control (n=3) and *Lrit2*$^{-/-}$ (n=3) mice at 1M. Representative scotopic **(D)** and photopic **(E)** ERGs elicited by four different stimulus intensities in WT and *Lrit2*$^{-/-}$ mice. Scotopic and photopic ERGs of *Lrit2*$^{-/-}$ mice were similar to those of WT.

(F) Immunostaining analysis of WT and *Lrit2*$^{-/-}$ retinas with retinal cell or synaptic markers as follows: the anti-Grm6 (green) and anti-Calbindin (red) (upper panels), anti-PKC□ (green) and anti-Ctbp2 (red) (middle panels), and anti-Pikachurin (green) and anti-Lrit1 (red) (lower panels). Nuclei were stained with DAPI (blue). ONL, outer nuclear layer; OPL, outer plexiform layer; INL, inner nuclear layer.

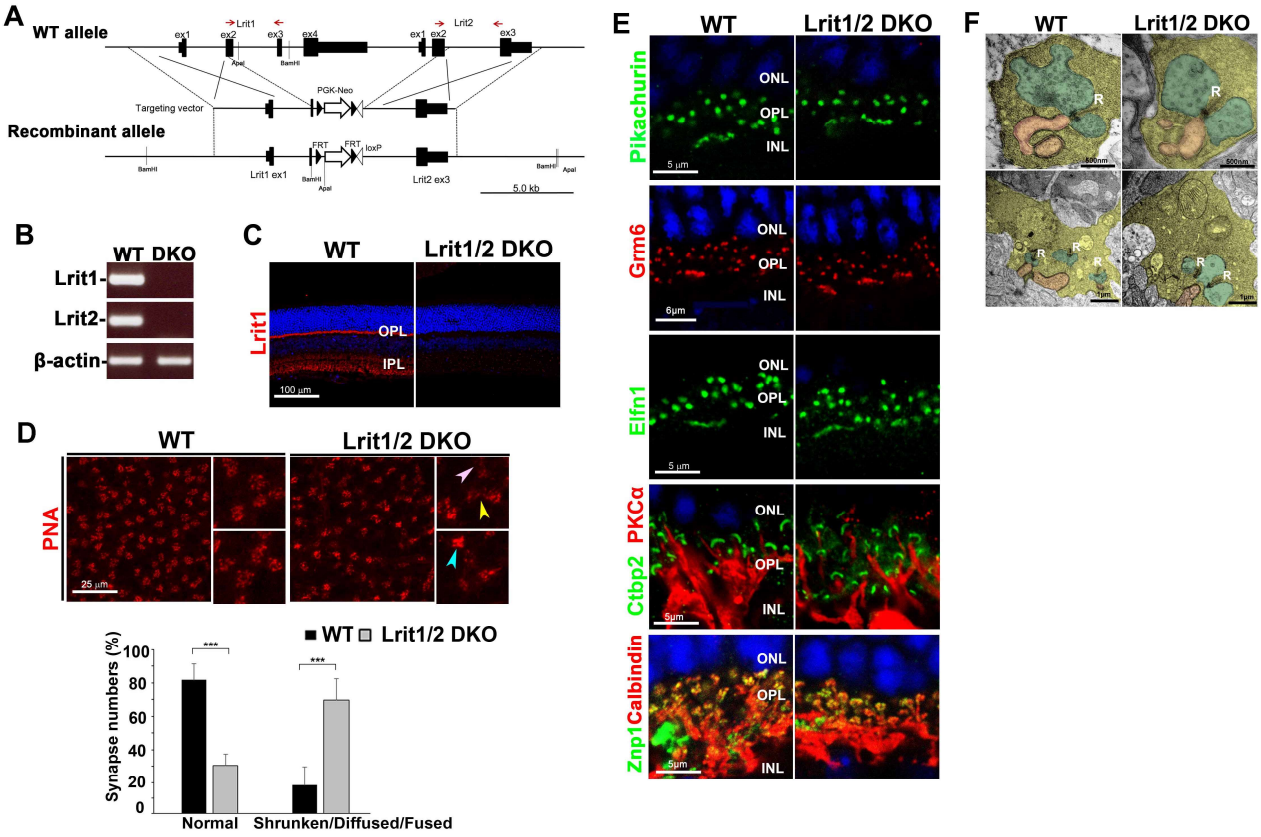

Figure S5. Morphological defects comparable to that in the *Lrit1*$^{gt/gt}$ retina were observed in the *Lrit1/2* DKO retina, Related to Figure 2.

(A) Schematic diagram of *Lrit1/2* DKO allele. The genomic region containing *Lrit1* exon 2-4 and *Lrit2* exon 1-2 was replaced with a *PGK-neo* cassette. Red arrows indicate primers to detect *Lrit1* or *Lrit2* allele in WT mice, respectively.

(B) RT-PCR analysis of *Lrit1* and *Lrit2* transcripts in the WT control and *Lrit1/2* DKO retinas. The primers for detection of *Lrit2* transcripts were designed within the *Lrit2* exon 2 and 3. No *Lrit1* or *Lrit2* transcripts were detected in the *Lrit1/2* DKO retina.

(C) Immunostaining of the WT and *Lrit1/2* DKO retina with the anti-Lrit1 antibody (red). The Lrit1 signal observed in the OPL and IPL of the WT disappeared in the *Lrit1/2* DKO retina.

(D) Flat-mount immunostaining of WT (n=3) and *Lrit1/2* DKO (n=4) retinas with PNA-rhodamine (red, upper panels). The percentages of normal and abnormal morphological cone photoreceptor synaptic terminals in WT and *Lrit1/2* DKO retinas was quantified (lower panel). Significantly decreased numbers of normal synapses and increased numbers of shrunken/diffuse/fused synapses were observed in the *Lrit1/2* DKO retina, as well as in the *Lrit1*$^{gt/gt}$ retina. Error bars show the SD. ***P<0.01.

(E) Immunohistological analysis of WT and *Lrit1/2* DKO retinas with retinal cell or

synaptic markers as follows: Pikachurin (photoreceptor synapse, green), Grm6 (red), Elfn1 (photoreceptor synapse, green), Ctbp2 (green) and PKCα (red), and Znp1 (green) and Calbindin (red). Nuclei were stained with DAPI (blue).

(F) Electron microscopic analysis of photoreceptor ribbon synapses in the OPL of the *Lrit1/2* DKO retina. No obvious change in synaptic invaginations was observed between WT and *Lrit1/2* DKO retinas. Photoreceptor axonal terminals are colored in yellow, horizontal cell processes in green, and bipolar cell dendrites in pink. ONL, outer nuclear layer; OPL, outer plexiform layer; INL, inner nuclear layer; IPL, inner plexiform layer; R, synaptic ribbon.

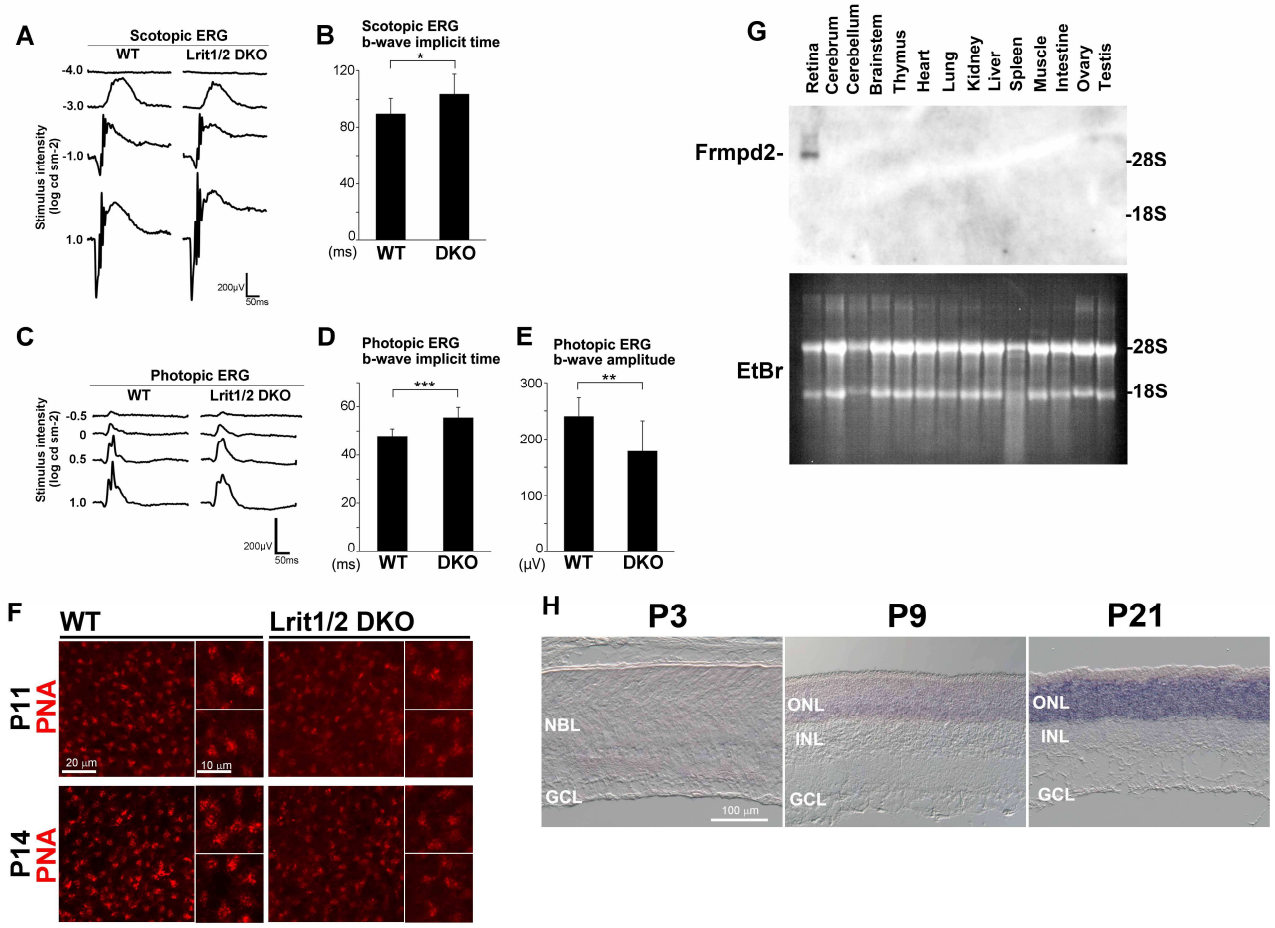

Figure S6. ERG defects in *Lrit1/2* DKO mice and Frmpd2 expression in developing and mature mouse retinas, Related to Figure 3 and 5.

(A-E) ERGs recorded from WT control (n=7) and *Lrit1/2* DKO (n=9) mice at 1M. Representative scotopic **(A)** and photopic **(C)** ERGs elicited by four different stimulus intensities in WT and *Lrit1/2* DKO mice. The implicit times of scotopic b-wave as a function of the stimulus intensity (1.0 log cd sm^{-2}) **(B)** and photopic ERG b-wave as a function of the stimulus intensities (0.5 and 1.0 log cd sm^{-2}) **(D)** were prolonged in *Lrit1/2* DKO mice. The amplitude of the photopic ERG b-wave as a function of the stimulus intensity (1.0 log cd sm^{-2}) was decreased in *Lrit1/2* DKO mice **(E)**. Error bars show the SD. **P*<0.05, ***P*<0.03, ****P*<0.01

(F) Retinal flat-mount fluorescent staining of WT and *Lrit1/2* DKO mice at P11 and P14 with PNA-rhodamine (red). The morphological abnormalities of the PNA signals were observed in the *Lrit1/2* DKO retina at both P11 and P14.

(G) Northern blot analysis of the *Frmpd2* transcript in the 1M mouse tissues. The distribution of *Frmpd2* mRNA among mouse tissues (upper panel) and ethidium bromide (EtBr) staining of the RNA (lower panel) were shown. 18S and 28S rRNAs were indicated.

Frmpd2 is specifically expressed in the retina, as is *Lrit1*.
(H) *In situ* hybridization of *Frmpd2* in developing (P3, P9) and mature (P21) mouse retinas. *Frmpd2* expression was observed specifically in photoreceptor cells at P9 and P21, but not at P3. NBL, neuroblastic layer; ONL, outer nuclear layer; INL, inner nuclear layer; GCL, ganglion cell layer.

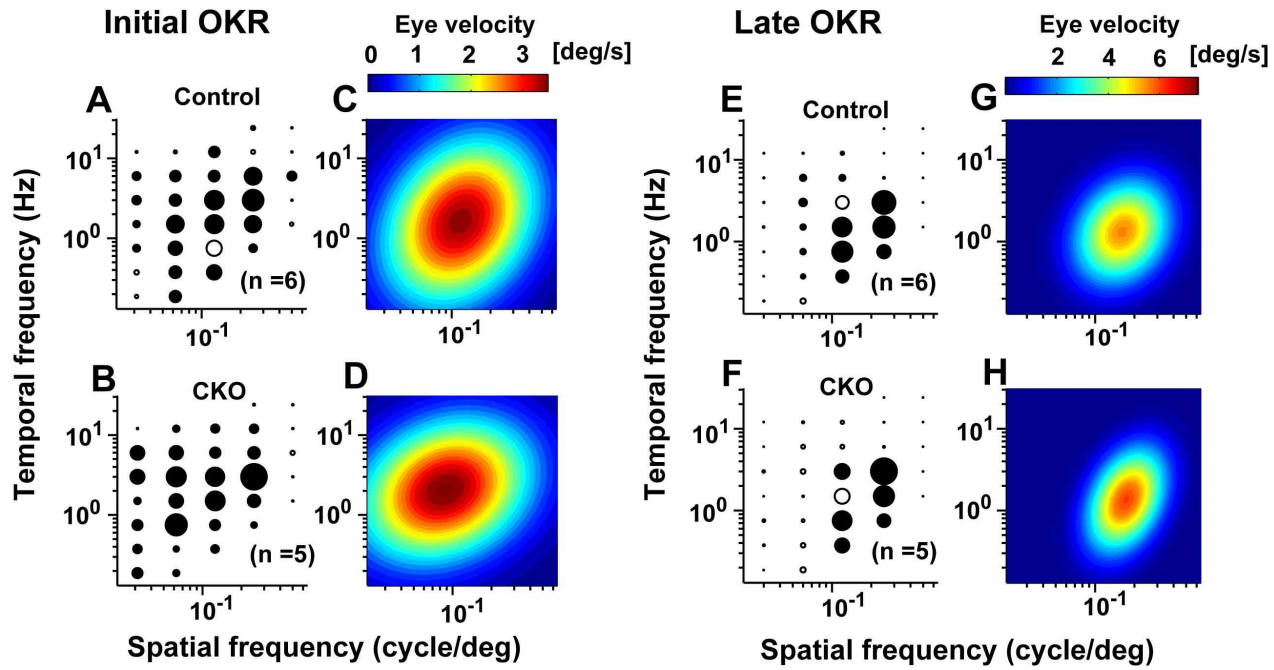
Initial OKR
Eye velocity
0 1 2 3 [deg/s]
A Control
C
B CKO
D
(n =6)
(n =5)
Temporal frequency (Hz)
Spatial frequency (cycle/deg)
Late OKR
Eye velocity
2 4 6 [deg/s]
E Control
G
F CKO
H
(n =6)
(n =5)
Temporal frequency (Hz)
Spatial frequency (cycle/deg)

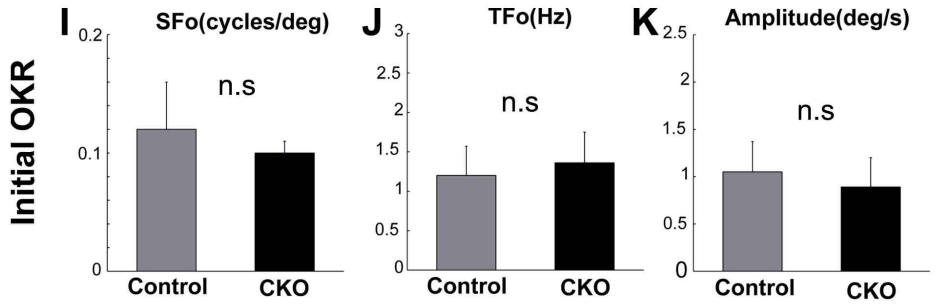
Initial OKR
I SFo(cycles/deg)
n.s
J TFo(Hz)
n.s
K Amplitude(deg/s)
n.s
Control
CKO

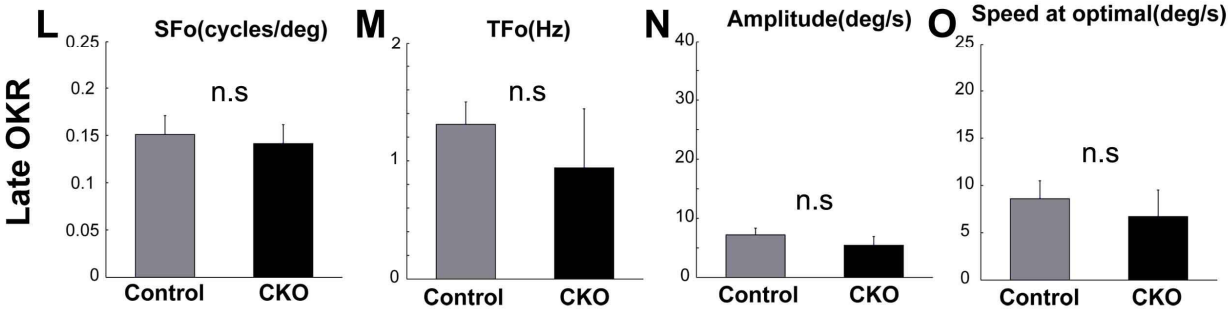
Late OKR
L SFo(cycles/deg)
n.s
M TFo(Hz)
n.s
N Amplitude(deg/s)
n.s
O Speed at optimal(deg/s)
n.s
Control
CKO

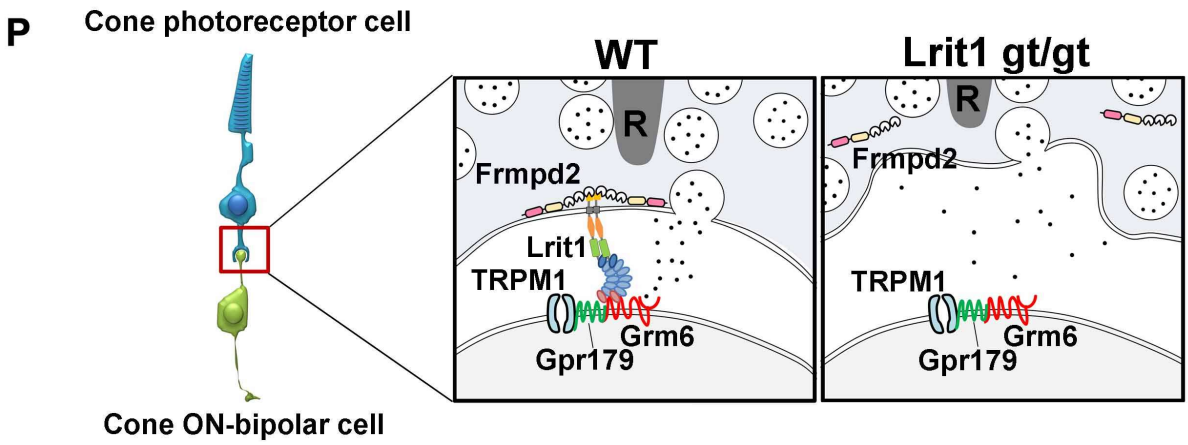
P
Cone photoreceptor cell
WT
Lrit1 gt/gt
R
Frmpd2
Lrit1
TRPM1
Grm6
Gpr179
Cone ON-bipolar cell

Figure S7. OKRs in the ON bipolar-specific *Lrit1* CKO mice were not affected, Related to Figure 6.

(A, B) Amplitudes of the initial OKRs in control and ON bipolar-specific *Lrit1* CKO mice are represented by the diameter of circles plotted in the coordinate system of SF and TF.

(C, D) Heat-map plots of the best-fit Gaussian functions for the initial OKRs in control and *Lrit1* CKO mice are presented.

(E, F) Amplitudes of the late OKRs in control and *Lrit1* CKO mice represented by the diameter of circles plotted in the coordinate system of SF and TF.

(G, H) Heat-map plots of the best-fit Gaussian functions for the late OKRs in control and *Lrit1* CKO mice are presented.

(I-K) Comparisons of the properties of the initial OKRs in control (n=6) and *Lrit1* CKO (n=5) mice. The optimal spatial frequency **(I)**, temporal frequency **(J)** and amplitude **(K)** in initial OKRs in control and *Lrit1* CKO mice are shown.

(L-O) Comparisons of properties of the late OKRs control (n=6) and *Lrit1* CKO (n=5) mice. The optimal spatial frequency **(L)**, temporal frequency **(M)**, amplitude **(N)**, and speeds at the optimal stimulus **(O)** in late OKRs in control and *Lrit1* CKO mice are shown.

(P) A proposed model of the Lrit1 function in cone photoreceptor-cone ON-bipolar cell synapses. Lrit1 regulates synapse formation between photoreceptor and cone ON-bipolar cells by interacting with Frmpd2 through its intracellular domain as well as with Grm6 in *trans* through the extracellular domain, respectively (WT, left panel). Trpm1 is the retinal ON-bipolar cell transduction channel in the Grm6 cascade. Gpr179, a member of the G protein-coupled receptor superfamily, forms a complex with Trpm1 and Grm6. Lrit1-Grm6 trans-synaptic interaction may facilitate synapse formation of photoreceptor and cone ON-bipolar cells. In the *Lrit1*$^{gt/gt}$ retina (right panel), loss of Lrit1 affects Frmpd2 localization in photoreceptor synaptic terminals and causes synaptic structure abnormalities in photoreceptor cells as well as signal transmission impairment from photoreceptors to cone ON-bipolar cells. Error bars show the SD.

Acknowledgments

I thank Dr. Kirill A. Martemyanov (The Scripps Research Institute) for providing the anti-Elfn1 antibody, T. Ryu for help with the experiments, M. Kadowaki, A. Tani, A. Ishimaru, Y. Tohjima, K. Hasegawa, T. Tsujii, H. Abe, and S. Kennedy for technical assistance. This work was supported by CREST (A-MED), Grant–in-Aid for Scientific Research (B) (15H04669) and (C) (16K08583), Young Scientists (B) (15K189550) from the Japan Society for the Promotion of Science (JSPS), The Takeda Science Foundation, Senri Life Science Foundation, The Sumitomo Foundation, Suzuken Memorial Foundation, KANAE Foundation for the Promotion of Medical Science, Terumo Foundation for Life Science and Arts Life Science support program, and Center for Medical Research and Education, Graduate School of Medicine, Osaka University.

Achievements

Journal

Takahisa Furukawa, Akiko Ueno, Yoshihiro Omori. Molecular mechanisms underlying selective synapse formation of vertebrate retinal photoreceptor cells. *Cell Mol Life Sci,* 2019, Oct 4, [Epub ahead of print].
論文執筆、図の作製に携わった

Akiko Ueno, Yoshihiro Omori, Yuko Sugita, Satoshi Watanabe, Taro Chaya, Takashi Kozuka, Tetsuo Kon, Satoyo Yoshida, Kenji Matsushita, Ryusuke Kuwahara, Naoko Kajimura, Yasushi Okada, Takahisa Furukawa. Lrit1, a Retinal Transmembrane Protein, Regulates Selective Synapse Formation in Cone Photoreceptor Cells and Visual Acuity. *Cell Reports*, 2018, Mar 27; 22(13): 3548-3561

Cesare Orlandi, Yoshihiro Omori, Yuchen Wang, Yan Cao, Akiko Ueno, Michel J.Roux, Giuseppe Condomitti, Jorisde Wit, Motoi Kanagawa, Takahisa Furukawa, Kirill A.Martemyanov. Transsynaptic Binding of Orphan Receptor GPR179 to Dystroglycan-Pikachurin Complex Is Essential for the Synaptic Organization of Photoreceptors. *Cell Reports*, 2018, Oct 2; 25(1): 130-145.
一部の ERG の測定と解析、免疫組織染色に携わった

Yoshihiro Omori, Shun Kubo, Tetsuo Kon, Mayu Furuhashi, Hirotaka Narita, Taro Kominami, Akiko Ueno, Ryotaro Tsutsumi, Taro Chaya, Haruka Yamamoto, Isao Suetake, Shinji Ueno, Haruhiko Koseki, Atsushi Nakagawa, Takahisa Furukawa. Samd7 is a cell type-specific PRC1 component essential for establishing retinal rod photoreceptor identity. *Proc Natl Acad Sci U S A*, 2017, Sep 26; 114(39): E8264-E8273.
Yeast-2-hybrid スクリーニングに携わった

Meriam Boubakri, Taro Chaya, Hiromi Hirata, Naoko Kajimura, Ryusuke Kuwahara, Akiko Ueno, Jarema Malicki, Takahisa Furukawa, Yoshihiro Omori. Loss of ift122, a Retrograde Intraflagellar Transport (IFT) Complex Component, Leads to Slow, Progressive Photoreceptor Degeneration Due to Inefficient Opsin Transport. *J Biol Chem*, 2016, Nov 18; 291(47): 24465–24474.
ゼブラフィッシュの作製、飼育に携わった

Conference

Akiko Ueno

Leucine-rich repeat proteins Lrit1 and Lrit2 regulate synapse formation in retinal photoreceptors.

第 15 回蛋白質研究所リトリート、大阪大学、2016 年 11 月 20 日 (Oral)